

migration as potential driving forces. The scale of the melt fraction variations and the speed at which they develop appear compatible with the thermal migration model.

PATTERNS AND MECHANISMS OF MELT DISTRIBUTION IN PARTIALLY
MOLTEN HARZUGITE UNDER HYDROSTATIC PRESSURE

By

Jiangyi Hou

Thesis submitted to the Faculty of the Graduate School of the
University of Maryland, College Park, in partial fulfillment
of the requirements for the degree of
Master of Science
2016

Advisory Committee:

Associate Professor Wen-lu Zhu, Chair (University of Maryland)
Associate Professor Laurent G.J. Montési, Co-advisor (University of Maryland)
Assistant Professor Melodie French (Rice University)

© Copyright by
Jiangyi Hou
2016

Acknowledgements

This thesis work couldn't be done without the help from my advisors, Drs. Wenlu Zhu and Laurent Montési. You introduced me to the world of rock physics and geodynamics, and dedicated your time leading me along the path of becoming a geoscience researcher. Your passion and wisdom on geoscience deeply impressed and motivated me. I want to sincerely thank you for all of your guidance, patience and understanding.

Special thanks should also go to my committee member Dr. Melodie French from Rice University. Thanks for the help you gave me on my presentation and suggestions on my project. Also thanks for traveling a long way to attend my proposal and thesis defense.

I want to thank my role model Kevin Miller, who was a Ph.D. student in our group and is now a post-doc at Stanford University, for sharing his data and his knowledge on digital rock physics with me. I enjoyed your intelligence and easy going attitude during our past discussions on scientific problems. I want to thank Hailong Bai, for your helpful discussion on general geology and numerical geodynamics modeling. Your optimism has a great impact on me!

I want to thank my previous housemate and friend Fang Huang, who is a geochemistry Ph.D. student in Johns Hopkins University. I've broadened my view in geoscience simply through the everyday chat with you. Also you're like a big brother to me in everyday life, helping me adapt to American culture and lifestyle, giving me suggestions when I got in trouble.

I want to thank all the former and current members of the “Chinese Mafia” that I met in our department: Ming Tang, Huan Cui, Hailong Bai, Chao Gao, Tiange Xing, Quancheng Huang, Songjie Wang, Bin Xia and Meng Guo for all your help and support during the time we have been together. You’re my family here!

I want to thank my fiancée, Manyi Wang, for your continuous support, accompany and encouragement. I want to thank my parents, who I haven’t united with for the past two and a half years, for all of your care, understanding and love from the other side of the Earth.

Table of Contents

Acknowledgements.....	ii
Table of Contents.....	iv
List of Tables.....	vi
List of Figures.....	vii
Chapter 1: Introduction.....	1
1.1 Melt Generation at Mid-Ocean Ridges.....	2
1.2 Melt Segregation.....	3
1.3 Melt Channelization.....	7
Chapter 2: Data Acquisition and Analyzing Methods.....	9
2.1 Experimental Overview.....	9
2.2 Subvolume Selection.....	12
2.3 Image Denoising and Segmentation.....	13
2.3.1 Segmentation of Melt Phase.....	15
2.3.2 Segmentation of Mineral Phases.....	18
Chapter 3: Result of Melt and Mineral Distribution.....	26
3.1 Vertical Melt Fraction.....	29
3.1.1 Time Series.....	29
3.1.2 Regular Series.....	30
3.2 Horizontal Melt Fraction.....	33
3.3 Opx/Olivine Fraction.....	33
Chapter 4: Discussion.....	44
4.1 Buoyancy-Dirven Melt Migration.....	44
4.2 Surface Tension Driven Melt Migration.....	46
4.3 Lithologic Partitioning.....	48
4.4 Thermal Migration.....	50
Chapter 5: Conclusion.....	54
Appendix A.....	57
Appendix B.....	60

Appendix C	69
Bibliography	73

List of Tables

Table 2.1: Experimental conditions and detection of an upward melt fraction increase	10
Table A.1: Notations of variables used in McKenzie governing equations	59
Table B.1: List of location, size, analysis directions and methods of all analyzed subvolumes	61

List of Figures

Figure 1.1: Illustration of the adiabatic decompressing upwelling process	3
Figure 1.2: Idealized cross-section of a melt in contact with three grains.....	5
Figure 2.1: Schematic diagram illustrating the preparation of samples and the acquisition of X-ray Synchrotron microtomographic data	11
Figure 2.2: Horizontal slice of 3-D microtomographic reconstruction of sample hzb-15.....	13
Figure 2.3: Iterative top-hat segmentation	17
Figure 3.1: Vertical melt fraction heterogeneity.....	27
Figure 3.2: Horizontal variation in melt fraction in horizontally-cored sample hzb-228	
Figure 3.3: Vertical variation of melt fraction for sample hzb6-10.....	31
Figure 3.4: Vertical variation of melt fraction for samples with different nominal melt fractions or olivine/opx ratio.....	32
Figure 3.5: Horizontal melt variation for different sample subvolumes.....	33
Figure 3.6: Melt and mineral volume fraction along hzb-6 sample core axis	35
Figure 3.7: Melt and mineral volume fraction along hzb-7 sample core axis	36
Figure 3.8: Melt and mineral volume fraction along hzb-9 sample core axis	37
Figure 3.9: Melt and mineral volume fraction along hzb-10 sample core axis	38
Figure 3.10: Melt and mineral volume fraction along hzb-15 sample core axis	39
Figure 3.11: Melt and mineral volume fraction along hzb-14 sample core axis	40
Figure 3.12: Melt and mineral volume fraction along hzb-12 sample core axis	41
Figure 3.12: Melt and mineral volume fraction along hzb-5 sample core axis	42
Figure 3.13: Melt and mineral volume fraction along hzb-2 sample core axis	43
Figure 4.1: Schematic figure of minimum energy melt fractions for a system with melt and different minerals	49
Figure 4.2: Schematic phase diagram illustration for saturation gradient chemical diffusion and Soret diffusion	51
Figure C.1: Segmentation of hzb5-sub1 by Grain Separation	70
Figure C.3: Grain separation segmentation result of hzb15-sub1.....	72

Chapter 1: Introduction

Melting of mantle rocks occurs beneath mid-ocean ridges, along subduction zones and hotspots. Mid-ocean ridges, which feature the spreading centers where lithospheric plates are created, are a fundamental component of plate tectonics. Upwelling hot mantle causes partial melting starting at a depth of a few tens of kilometers beneath the mid-ocean ridge (e.g. Langmuir et al., 1992). As the melt ascends to the ridge, it cools and crystalizes to form new basaltic oceanic crust. Numerous studies have been done on melt migration beneath the ridges from geophysical, geochemical and geological perspectives (MELT Seismic Team, 1998; Evans et al., 1999; Kelemen et al., 1997; Niu, 1997; Key et al., 2013; Gale et al., 2014) and models have been developed to describe the melt flow through the mantle scale based on the micro physics of melt migration (e.g., Spiegelman & McKenzie, 1987; Katz, 2008; Montési et al., 2011; Bai & Montési, 2015; Turner et al., 2016). However, not every aspect of the melt extraction system at mid-ocean ridges is well understood. For example, it is clear from geological and geochemical observations that melt utilizes high-permeability conduits, possibly dunite bodies, to increase melt extraction velocities (Kelemen et al., 1997; Miller et al., 2014). In this thesis, I study heterogeneities in melt content that developed spontaneously in partially molten harzburgite samples to evaluate whether they might represent a phenomenon that facilitates melt extraction at large scale.

In what follows, I first review melt migration at mid-ocean ridges, including an outline of the main theories and evidence for channeled melt flow. Then I describe the methods I am using to characterize melt and mineral distribution in experimental partially molten harzburgite samples. After describing the results to date, I discuss possible physical origins of the observed variations and implications from them.

1.1 Melt Generation at Mid-Ocean Ridges

The state of a material depends on environmental conditions such as pressure and temperature. The upper mantle is constituted principally of peridotite, a rock composed of olivine and orthopyroxene (opx). Temperature increases approximately linearly with depth due to the adiabatic self-compression of rocks under pressure, which also increases approximately linearly with depth due to gravity. At intraplate regions, the temperature at the base of the lithosphere is not sufficient to cause significant melting, although volatiles like water and CO₂ can generate small amounts of melt (Asimow & Langmuir, 2003; Dasgupta & Hirschmann, 2006). At mid-ocean ridges, two lithospheric plates on either side of the ridge move away from each other. Warm asthenosphere rises underneath the ridge axis under progressively decreasing pressure. The pressure drop during the mantle upwelling occurs faster than the heat exchange with surrounding rocks, thus the process is considered as adiabatic and carries minerals in peridotite across their solidus (see [Figure 1.1](#), *Geodynamics* by Turcotte & Schubert, 2002), causing partial melting. The process is known as the decompression melting or pressure-release melting. If the mantle trajectory is described by corner flow theory (McKenzie, 1969), melting at a mid-ocean ridge is expected to take place in triangular

region beneath the ridge axis (Reid & Jackson, 1981; Langmuir et al., 1992). Although the depth and width of the melting region observed using geophysical data are consistent with this model (MELT Seismic Team, 1998; Evans et al., 1999), the melt is more uniformly distributed than expected and is present in surprisingly small amounts: only one to two percent volume fraction compared the more than 10% expected degree of melting. The difference implies an efficient melt extraction system reaching several tens of kilometers into the mantle.

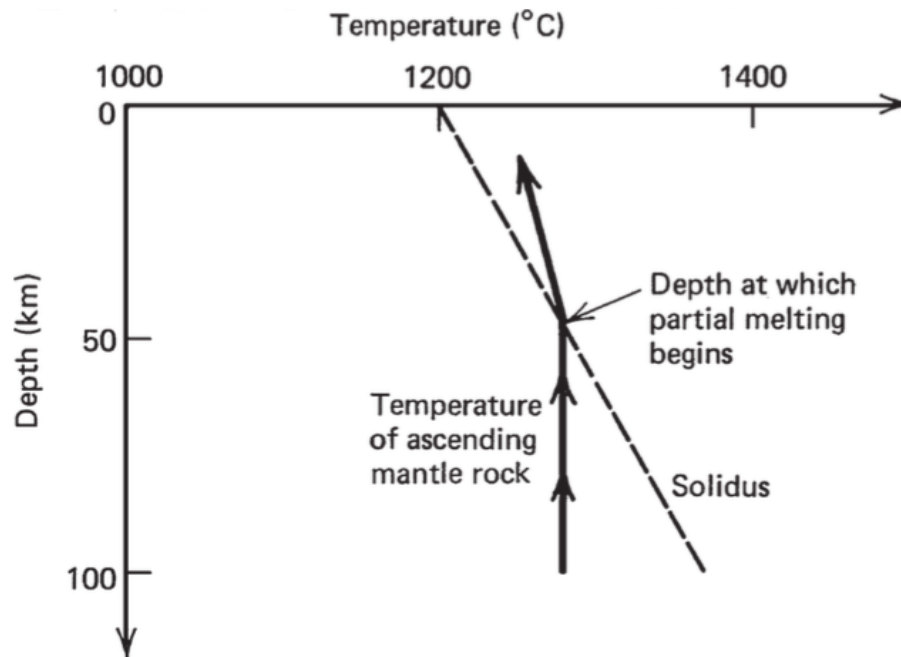


Figure1.1: Illustration of the adiabatic decompressing upwelling process. Partial melting occurs as the adiabatic ascent carries the hot mantle rock across its solidus. Figure from *Geodynamics* by Turcotte and Schubert (2002).

1.2 Melt Segregation

Melt segregation refers to the process by which melt is extracted from a partially molten region and results in the upward migration of melt to the earth's surface (e.g.

McKenzie, 1984). Segregation requires that the partially molten peridotite is permeable enough for melt to flow through relatively easily.

Experimental observations on melt microstructure in partially molten aggregates show that the melt spreads out along grain edges and infiltrates three-grain junctions (triple-junctions) under hydrostatic stress (Bulau et al., 1979; Waff & Balau, 1979). Local variations in the solid-solid and solid-melt interfacial energies control melt distribution at grain scale (Waff & Bulau, 1979; Cooper & Kohlstedt, 1982). Given sufficient time and a constant hydrostatic pressure, the system approaches a steady equilibrium state (textural equilibrium) as it reorganizes to minimize the total interfacial energy. The condition for equilibrium of an ideal two-phase system is expressed by the equation of the dihedral angle (Eq.1).

$$\cos\left(\frac{\theta}{2}\right) = \frac{\gamma_{ss}}{2\gamma_{sl}} \quad (1)$$

where θ is the dihedral angle, defined as the angle subtended between two solid-liquid interfaces (Figure 1.2), γ_{ss} is the interfacial energy at solid-solid contact, and γ_{sl} is the interfacial energy of the solid-liquid interface. Eq.1 bridges the thermodynamic parameters with a geometrical parameter and makes the dihedral angle experimentally measurable. Cooper & Kohlstedt (1982) measured the dihedral angles between basaltic melt and two olivine grains and obtained an anisotropic solid-liquid interfacial energy ranging from 0.5 to 1.6 J/m². Several experiments were conducted to measure the dihedral angle between olivine-olivine, olivine-basalt, and opx-basalt interfaces at different temperatures and pressures. A summary of results (Harte et al., 1993) shows that the dihedral angles between olivine grains and basaltic, komatiitic and carbonatitic melts are between 25° and 40°. With such low dihedral angles, even a small melt

fraction (1%~5%) leads to 3-dimensional (3-D) connected melt network and percolates through the rock. Zhu et al. (2011), using X-ray synchrotron microtomography, confirmed that basalt in an olivine matrix remains well connected even at melt fractions as small as 2%, similar to the melt fraction typically observed at mid-ocean ridges. This interconnected melt network implies that a partially molten aggregate can be considered as a porous medium saturated with melt and that the melt obeys porous flow equations.

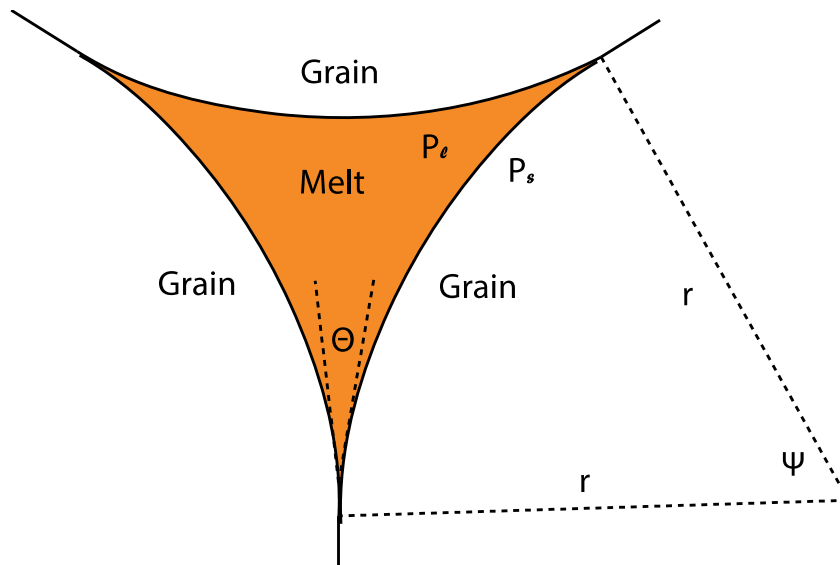


Figure 1.2: Idealized cross-section of a melt in contact with three grains. θ is the dihedral angle. P_f is the fluid pressure, P_s is the pressure in the grains, and r is the radius of curvature of the melt /solid interface. By symmetry $\Psi=\pi/3$.

The porous flow idea led Frank (1968) and Ahern & Turcotte (1979) to use Darcy's law to model melt migration in the upper mantle. Darcy's law is an empirical formula that links the velocity of the fluid, w , relative to that of the matrix, W , to the fluid pressure gradient ∇P_f , the permeability of the porous media, K , the melt viscosity μ , and porosity ϕ . If the fluid pressure gradient is due mostly to the difference in density

between solid and fluid, $\Delta\rho$, then $\nabla P_f = \Delta\rho g$, with g the acceleration of gravity, and Darcy's law becomes:

$$\phi(w - W) = \frac{K}{\mu} \Delta\rho g \quad (2)$$

Sleep (1974) and McKenzie (1984) pointed out that Darcy's law is insufficient to fully describe the segregation of melt because it ignores compaction and decompaction of the solid matrix in response to changes of pressure. McKenzie (1984) and later Bercovici et al., (2001) proposed two-phase flow models that regard the melt and the solid matrix as two interpenetrating viscous fluids. Mass and momentum conservation are treated using averaging theory (Drew and Segel, 1971; Drew, 1971). Stevenson and Scott (1987) independently arrived at a similar set of equations through conservation of energy. The most important parameter that controls the behavior of melt in this theory is the compaction length δ_c , given by

$$\delta_c = \sqrt{\frac{K(\zeta + \frac{4\eta}{3})}{\mu}} \quad (2)$$

where ζ and η are the bulk and shear viscosities of the melt/solid aggregate.

The compaction length is the length scale over which pressure gradients can be supported by the rigidity of the matrix. Compaction can be neglected at length scales larger than δ_c , but dominates at smaller length scales. For example, consider a one-dimensional column (Equations given in Appendix A). Melt rises under the influence of buoyancy and accumulates at the base of an impermeable layer. The thickness of the boundary layer in which melt accumulates is approximately the compaction length. Porosity in that boundary layer increases exponentially over time as the matrix

decompacts in response to the mounting melt pressure. Such a decompaction layer may be present along the base of the lithosphere at mid-ocean ridges and help focus toward the ridge axis melt that would otherwise simply rise vertically and contribute to the crustal budget even hundreds of kilometers from the axis (Sparks and Parmentier, 1991).

1.3 Melt Channelization

Trace element disequilibrium between mid-ocean ridge basalt (MORB) and abyssal peridotite and ophiolite suggests that melt transport should be relatively quick so that the melt didn't reach chemical equilibrium while traveling through the mantle. Dunite channels in ophiolite are in equilibrium with MORB, suggesting that the fast transport of melt takes place through these dunite bodies and that they act as chemically isolated channels (Kelemen et al., 1997).

Two mechanisms have been proposed to explain the development of these melt channels based on a feedback between melt fraction and 1) viscosity (Stevenson, 1989) or 2) melt-rock reaction (Kelemen et al., 1995). (1) Considering that the viscosity of a two-phase aggregate decreases with melt content or shear stress, as has been demonstrated experimentally (Kohlstedt, 2002), a high porosity region is weak, which reduces pressure and attracts melt according to Darcy's law, further increasing porosity. This feedback process is enhanced in presence of external shear (Katz et al., 2006) and has been demonstrated experimentally (Holtzman & Kohlstedt, 2003; 2007). (2) The solubility of clinopyroxene (cpx) in basaltic melts increases as the pressure decreases. Therefore, as the melt rises upward, the decreasing pressure enhances the dissolution

of cpx, which generates more porosity and permeability, increasing the upward melt velocity (Kelemen et al., 1995). This instability has been analyzed theoretically (Spiegelman et al., 2001) and can explain the tabular geometry of dunites in ophiolite as well as the diversity of trace element in melt inclusions at mid-ocean ridges (Spiegelman & Kelemen, 2003).

Permeability is the key physical parameter controlling the speed of melt transport but it has proven to be difficult to measure experimentally (Riley & Kohlstedt, 1990, 1991; Renner et al., 2003; Connolly et al., 2009). Miller et al. (2014) simulated fluid flow through partially molten olivine-basalt aggregates using the 3-D melt microstructure obtained by X-ray synchrotron microtomography and estimated that their permeability ranges from 2×10^{-16} to 3×10^{-13} m² for porosity of 0.02 to 0.20. When extrapolated to the asthenospheric mantle, these permeabilities allow melt to travel upward at velocity of at least 1m/yr. Although rapid, this velocity needs to be enhanced to satisfy constraints on chemical disequilibrium and Uranium series decay (Kelemen et al., 1997). Taking into account the enhanced porosity of melt channels makes it possible to increase melt velocity to 100 m/yr and explain the preservation of geochemical disequilibria generated at the base of the melting region (Miller et al., 2014).

Chapter 2: Data Acquisition and Analyzing Methods

The dataset used in my study is a representation of the melt and mineral distribution in experimentally produced aggregates of olivine, orthopyroxene (opx), and basaltic melt aggregates. I present here the methods used to generate, image, and analyze the samples.

2.1 Experimental Overview

Data of structural information of partially molten harzburgite samples were obtained from experiments by Miller et al., 2016. Synthetic harzburgite samples were prepared by isostatically hot-pressing powdered mixtures of oxides and natural basalt in a graphite capsule (Figure 2.1.1 A) at 1.5 GPa and 1350 °C for durations ranging from 42 hours to 2 weeks (Miller et al., 2016). The oxide mixture was adjusted to produce a specified olivine to opx volumetric ratio, either 60/40 or 82/18 (Table 2.1). Pulverized high alumina natural basalt was added in different proportions to the oxide mixtures to produce nominal melt fractions ranging from 0.02 to 0.20. The experimental charges were quenched immediately after sintering. Then the confining pressure was reduced. Cylindrical cores about 1.5 mm in diameter were drilled either parallel or perpendicular to the sample axis, which was vertical during sintering, and prepared for X-ray imaging (Figure 2.1 B, C).

Table 2.1: Experimental conditions and detection of an upward melt fraction increase

sample	olivine/opx volume ratio	nominal melt fraction	sintering duration (hours)	core orientation ²	increasing trend
hzb-2	82/18	0.10	168	perpendicular	No
hzb-3	82/18	0.05	168	Perpendicular	No
hzb-5	82/18	0.20	168	Parallel	Yes
hzb-6	82/18	0.05	42	Parallel	No
hzb-7	82/18	0.05	84	Parallel	No
hzb-9	82/18	0.05	168	Parallel	Yes
hzb-10	82/18	0.05	336	Parallel	ND ¹
hzb-12	60/40	0.10	200	Parallel	Yes
hzb-13	60/40	0.02	336	Parallel	Yes
hzb-14	60/40	0.20	200	Parallel	Yes
hzb-15	60/40	0.05	168	Parallel	Yes

¹ ND: not detectable due to the short length of the sample

² Cores are drilled either parallel or perpendicular to the cylindrical axis of the samples

X-ray synchrotron microtomography aims at constructing a three-dimensional representation of a sample without destroying it. The drilled core is placed in front of an X-ray beam. A scintillator converts the penetrating X-ray signal into visible light, which can be recorded by a CCD camera. The image corresponds to the density integrated along the X-ray path (Figure 2.1 D). The sample is rotated by 180° in 0.12° increment and a new image is recorded at each increment. The three-dimensional density field is reconstructed using the TomoPy software (Zhu et al., 2011; Gürsoy et al., 2014).

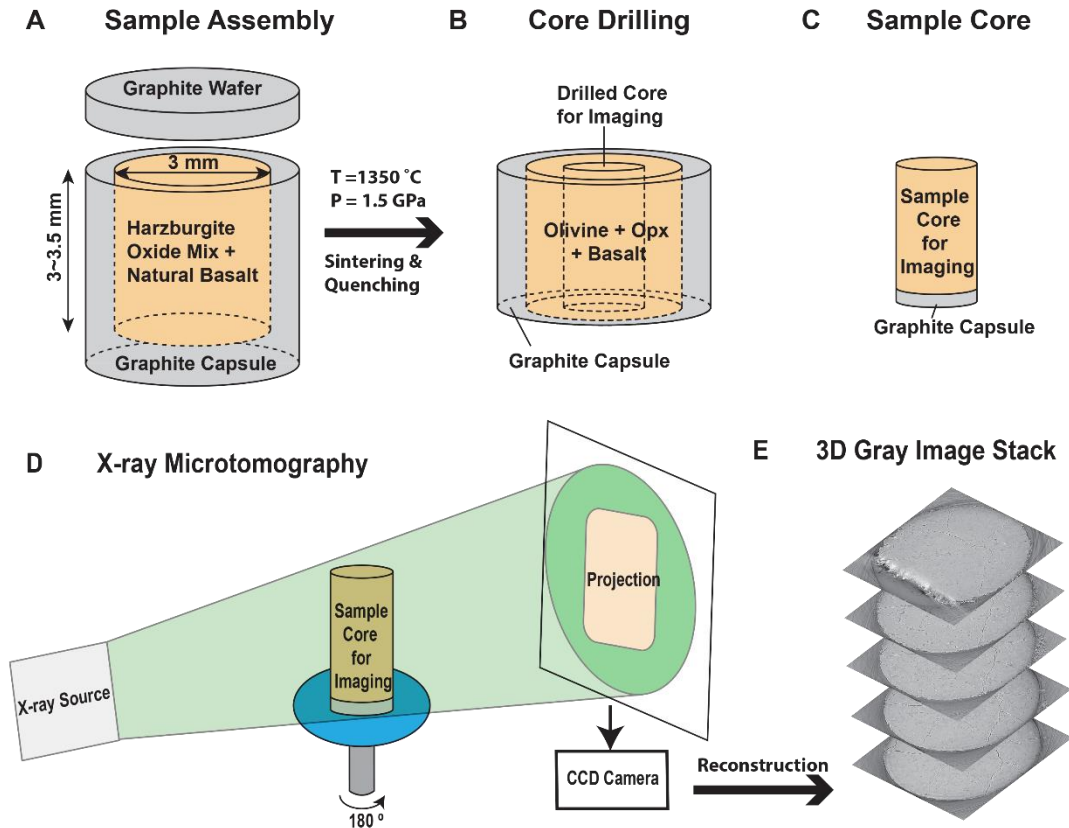


Figure 2.1: Schematic diagram illustrating the preparation of samples and the acquisition of X-ray Synchrotron microtomographic data. (A) Sample assembly before sintering. Powered oxides and natural basalt were homogeneously mixed (orange) and loaded in a graphite capsule (gray). (B) After sintering, the top of the sample was cut and polished and a core (C) was drilled from the remaining assembly, usually along the cylindrical axis of the sample. (D) The core was placed in a X-ray beam and the penetrating X-rays were converted to visible light by a scintillator and recorded by a CCD camera (from Miller et al. 2014). (E) 3D structure data of the sample core were organized as a stack of gray-scale images.

The three-dimensional data were organized as a stack of gray-scale images (Figure 2.1E). Each reconstructed sample core has about 2000 slices; each slice has 2048×2048 pixels with a resolution of 0.74 μm/pixel. The gray-scale intensity of each pixel is determined by the material density at that point; denser materials (olivine/opx grains) appear brighter than the less dense material (quenched basaltic melt), see Figure 2.2.

2.2 Subvolume Selection

The size of the data set collected for each sample core makes it impractical to analysis in entirety. Moreover, many samples broke during unloading and exhibit significant decompression cracks in the reconstructed image. Those cracks are void space generated after the sintering procedure and should not be counted into melt volume. We crop long and narrow column volumes (subvolumes) from each reconstructed digital sample to cover adequately a large volume of the sample while avoiding decompression cracks. The yellow square in [Figure 2.2](#) highlights, in horizontal slice of sample hzb-15, one acceptable subvolume. Multiple subvolumes with different sizes were cropped and analyzed for each sample. Subvolume definition was made by visual inspection of the 3-D image. The number and size of subvolumes varies sample to sample because of the variability of decompression crack development.

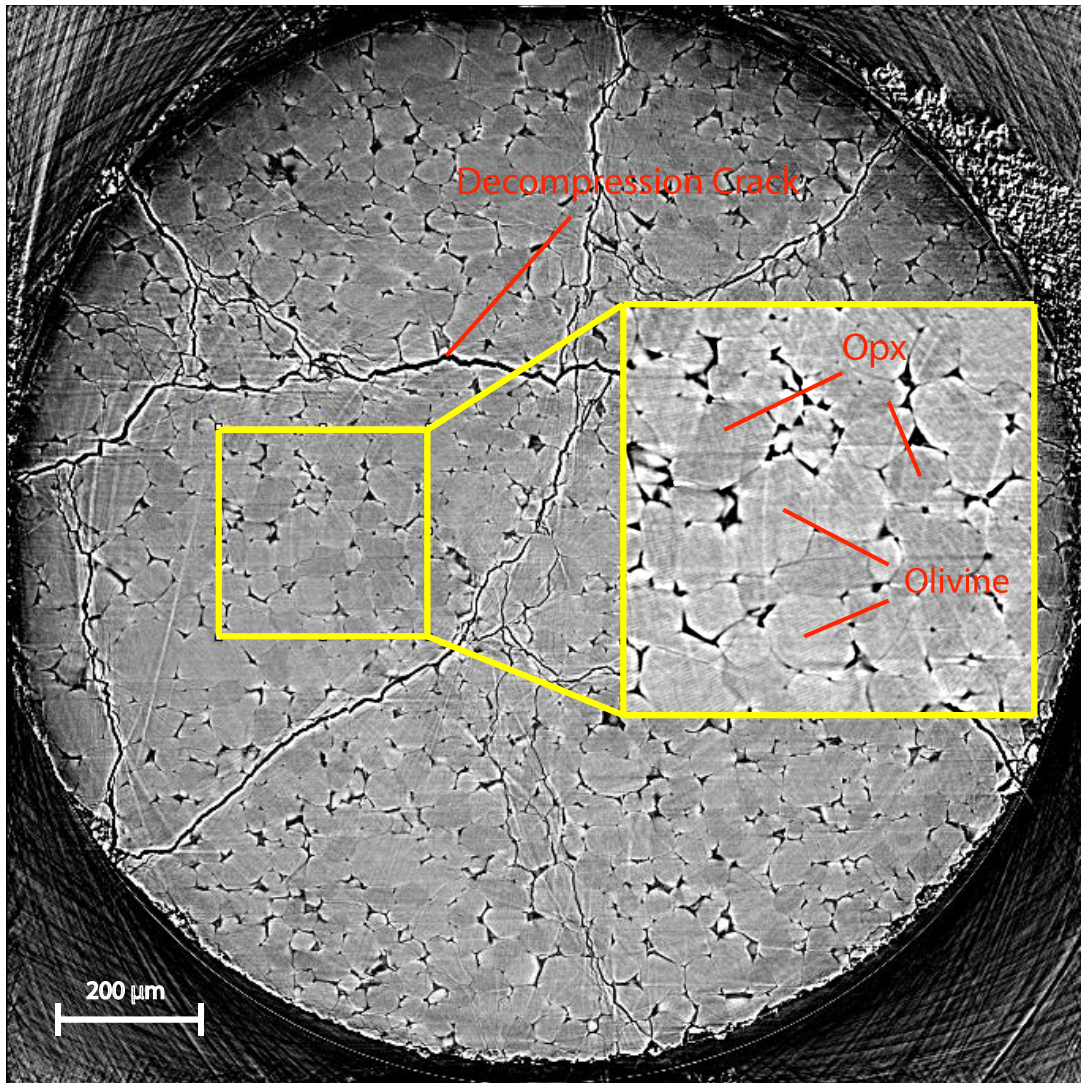


Figure 2.2: Horizontal slice of 3-D microtomographic reconstruction of sample hzb-15. The slice measures 2048 by 2048 pixels with a resolution of 0.74 microns. The yellow box outlines a subvolume of the dataset and inset contains a contrast-enhanced, zoomed-in view of the subvolume section. Olivine, opx and quenched basaltic melt (glass) appear as progressively darker material (labeled in inset). Decompression cracks appear as jagged dark line (empty space or air) with a bright outline.

2.3 Image Denoising and Segmentation

Quantitative analysis of the melt and mineral (olivine and opx) distribution in the partially molten harzburgite samples requires the spatial identification of each phase in the microtomographic dataset. This identification process involves image

segmentation, which involves partitioning an image into non-overlapping regions that represent different phases. Specifically, a segmentation process transforms the grayscale image into a labeled image, in which each phase is assigned an identification integer. The labeled images are then used as masks or computational domains for accurately calculating phase volume fraction and other physical rock properties.

However, the raw grayscale images are not immediately applicable for automatic segmentation. They contain white noise and imaging artifacts such as dark rings and dark slices, which could introduce unsatisfying segmentation results. A discussion of the imaging artifacts can be found in Boas & Fleischmann (2012). Dark slices are layers of slices that appear much darker than normal in the gray image stack. These dark slice layers appear occasionally in the stack and significantly affects the grayscale intensity based segmentation (segmentation is discussed in next section). To reduce the effect of dark slices, we calculate the mean grayscale intensity of the mineral phases (olivine + opx) in each slice of the subvolume, and rescale the grayscale intensity range of each slice with the ratio of local mean to global mean.

To reduce the importance of white noise, I first apply a non-local mean filter (Buades et al., 2005) to the raw grayscale image, which suppresses the white noise inside each phase while preserving the grain-melt interfaces. Several adjustable parameters strongly affect the results of the non-local mean filter: the search window size, the local neighborhood window size, and the similarity value. To determine the new grayscale value for the current voxel, the algorithm compares the neighborhoods (range of which determined by the neighborhood window size) of all voxels in the search window with the current voxel's neighborhood, looking for similarities between

the neighbors. The similarity determines the weight with which a voxel in the search window will affect the new value of the current voxel. Too small a search window size blurs the image because there isn't enough structural information within the searching area. Too large a search window size, however, is computationally expensive. We chose the default search window size of 21 pixels. Based on various trials, we decided that 2 to 10 pixels is a good range for the neighborhood window size. The similarity value determines the weight assigned to each voxel in the search window – the larger the value is, the more the image will be smoothed as a result. We use a default value of 0.6 for the similarity. Other edge-preserving filters like anisotropic diffusion filter are also used following the non-local mean filtering for further suppressing white noise in each phase.

2.3.1 Segmentation of Melt Phase

After reducing the noise to an acceptable level, a series of segmentation algorithms were implemented to the filtered gray images in the commercial software Avizo[®]. Three segmentation algorithms were tested and combined to process our data: gray-scale based global threshold segmentation, morphology-based top-hat segmentation and watershed segmentation.

The global threshold algorithm is based on thresholding the grayscale intensity. It sets a global grayscale intensity threshold level and labels pixels into two categories, which are respectively above or below the threshold. As the results purely depend on the grayscale intensity, dark or bright veins (artifacts due to the edge-enhancement

technique), dark rings (caused by miscalibrated or defective detector element), and long wavelength background variations can easily lead to unsatisfying segmentation results.

The top-hat transform is a morphology-based algorithm that extracts the local “hills” or “valleys” in the gray image. It can be considered as a local-thresholding method and is more reliable when processing data with long wavelength gray-scale variation. The top-hat segmentation module in Avizo® has several adjustable parameters such as kernel size and threshold. Large kernel size top-hat is better able to capture large-size features (e.g. wide melt pockets) while small kernel size is better able to capture thin and fine features. We apply the top-hat segmentations iteratively from large kernels to small kernels to capture both wide melt pockets and thin melt channels (Figure 2.3.1).

However, due to the complexity of artifacts in the gray images, none of those automatic segmentation methods is perfect. For example, dark ring artifacts can’t be eliminated by any of the three automatic segmentation modules. After the automatic segmentation, we manually check each slice and correct wrongly identified regions to more accurately capture of the spatial distribution of the melt. After the correction, all regions identified from different kernel sizes were merged into one as the final result of the melt phase segmentation (Figure 2.3 E).

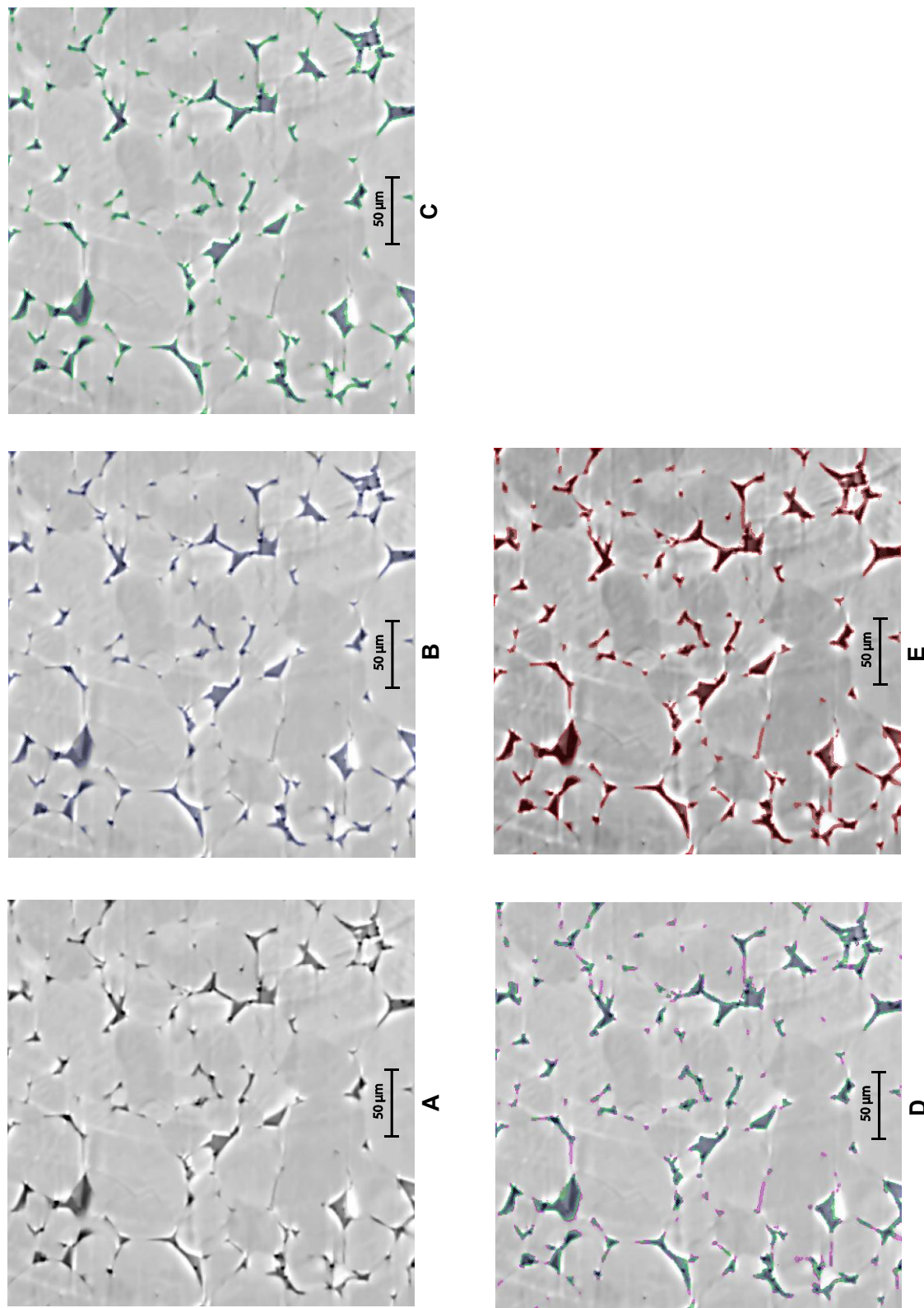


Figure 2.3: Iterative top-hat segmentation. (A) A slice of filtered grayscale image of one hzb-15 subvolume. (B) Regions of melt identified by the top-hat filter with kernel size 9 (dark blue); (C) Regions melt identified in the solid region of panel B by the top-hat filter with kernel size 5 (green); (D) Regions of melt identified in the solid region of panel C by the top-hat filter with kernel size 2 (purple); (E) Final segmentation result also including manual corrections to the automatically-segmented image. Note that the segmentation is conducted directly in 3D even though the visualizations here are only in 2D.

For each segmented subvolume, we calculate the melt fraction at different depths by counting the pixels assigned to the melt phase in each slice. In that way we obtain profiles of melt fraction against slice number, or equivalently the vertical position in the sample.

The uncertainty of the melt fraction measurement can be difficult to estimate. There are multiple sources of error. Errors can be introduced during imaging and reconstruction due to hardware defects or algorithms, and during the segmentation, due to discretization in the binary images. We estimate the uncertainty by morphologically shrinking (for the low bound) and dilating (for the high bound) the binary melt phase by one pixel (Fusseis et al., 2012; Miller et al., 2014). However, as pointed out by Fusseis et al. (2012), this error margins might significantly overestimate the true uncertainty. Segmentations obtained by global threshold, top-hat and watershed algorithms are identical within the uncertainty provided by the dilation and shrinking approach. Unless specified, all the results below were obtained using the successive top-hat method illustrated in [Figure 2.3](#).

2.3.2 Segmentation of Mineral Phases

The harzburgite samples also contains two solid mineral phases -- olivine and orthopyroxene (opx). To segment olivine and opx is much more difficult than segmenting melt and solids in the reconstructed microtomographic images. Because of the low contrast between olivine and opx, any white noise and/or image artifacts could cause severe ambiguity in distinguishing the two phases. In this study, I adopted two different methods, 1) the marker-based watershed segmentation (in Avizo[®]) and 2) the trainable Weka segmentation (in Fiji ImageJ), to segment olivine and opx.

2.3.2.1 Marker-based watershed segmentation

In image processing, the watershed of a gray image is analogous to the notion of a catchment basin and a height map. The watershed algorithm is a useful tool for separating connected features (olivine and opx grains in this case) based on the morphology of the landscape. The basic idea is to place a water source (also called watershed seed) in each regional minimum (valley) and flooding the catchment basin until the different water sources meet each other at the gradient peak (Figure 2.4). The algorithm is used to approximate the grain-grain boundaries which are sometimes ambiguous if only judged by grayscale intensity. Sometimes several adjacent valleys belong to the same grain and should be merged during the flooding. Thus, directly using the local minima as watershed seeds may yield unnecessary split in a single-phase region. In this study, I use marker-based watershed algorithm in Avizo[®] to segment olivine and opx, which allows me to set my own watershed seeds (markers) instead of using the local minima.

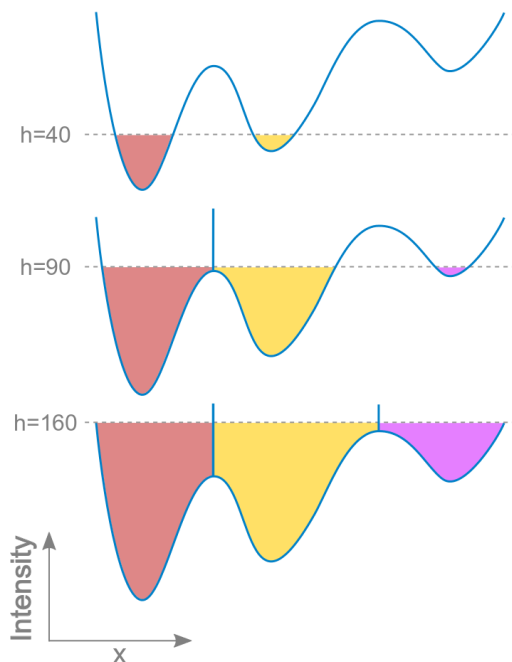
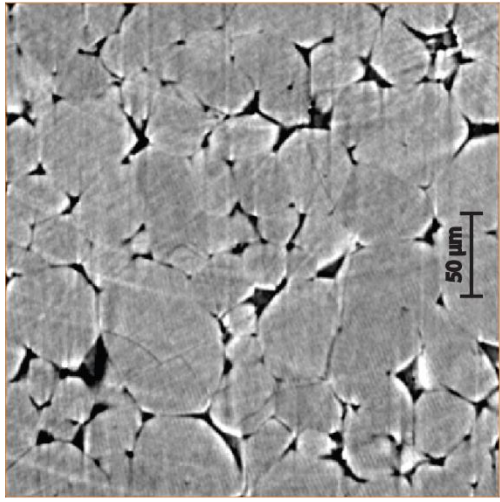


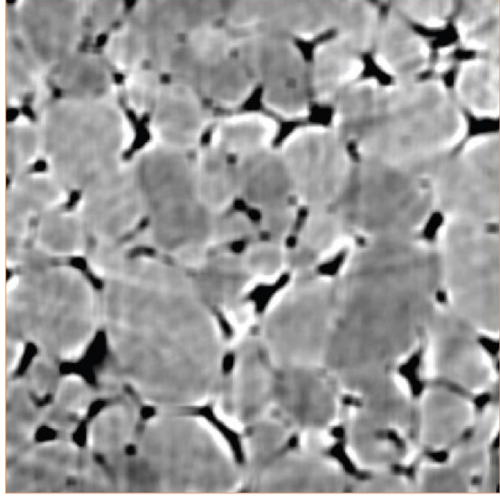
Figure 2.4 Schematic watershed flooding in 1D: Different water sources (labeled by different colors) are placed at the bottom of the valleys, i.e. local minima; then flooding starts from each water source and separated by the gradient peaks.

(http://imagej.net/Classic_Watershed)

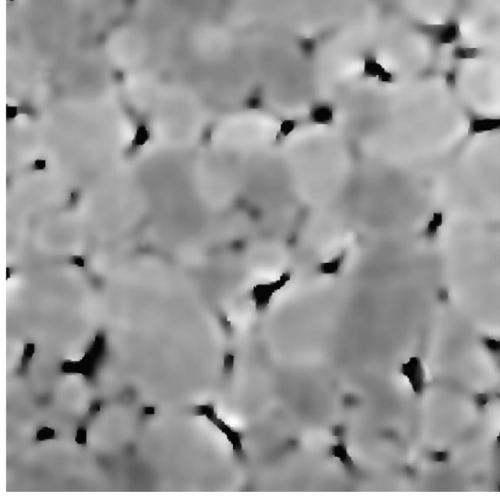
A series of filtering and thresholding are applied to the grayscale data to get proper seeds for the marker-based watershed segmentation. [Figure 2.5](#) is used to illustrate all the steps in the marker-based watershed segmentation for opx/olivine. First I apply a box filter to the grayscale images ([Figure 2.5A](#)) to get an overall suppression of white noise ([Figure 2.5B](#)). Secondly an anisotropic diffusion filter is applied to further smooth the inside of each phase. The resultant blurring of the grain boundaries is not a problem here because the focus of this step is to obtain the proper seeds for each phase ([Figure 2.5C](#)). After the filtering, an interactive threshold segmentation module is applied to conservatively label the darker area as the seed for opx ([Figure 2.5D](#)) and brighter area for olivine ([Figure 2.5 E](#)). The previous melt phase segmentation results are dilated and used as a mask in the above seed segmentation, and the interactive threshold for the seed is only applied in the unmasked area. Finally, the marker-based watershed segmentation module is implemented on the original grayscale image with the seeds as different markers and previous melt segmentation as a mask. The final result is shown in [Figure 2.5 F](#).



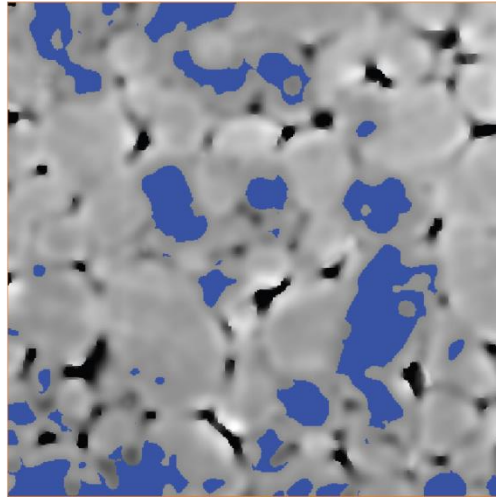
A. Original



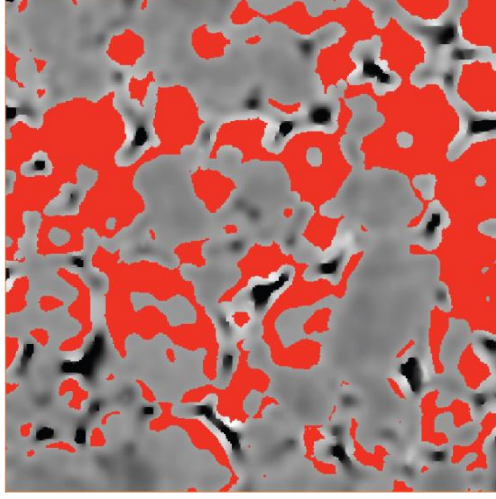
B. Box filtering



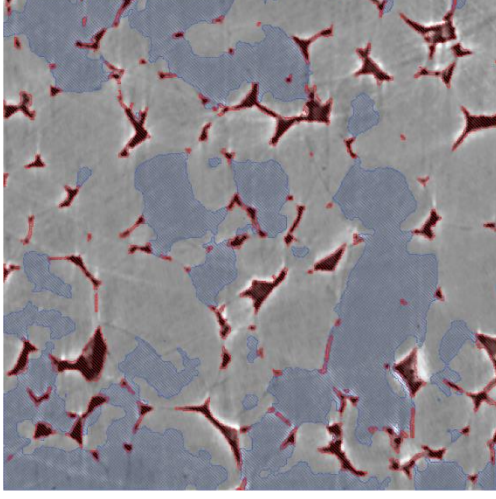
C. Anisotropic diffusion



D. Opx seed



E. Olivine seed



F. Watershed flooding

Figure 2.5: Marker-based watershed segmentation for opx/olivine. (A) A slice of grayscale image of one of hzb-15 subvolumes. (B) Apply a 3D box filter with kernel size = 8 pixel to A; (C) Apply 3D anisotropic diffusion filter to B; (D) Regions of opx identified from interactive thresholding (blue); (E) Regions of opx seed identified from interactive thresholding (red); (F) Watershed flooding and final segmentation result (red for melt; light blue for opx and rest for olivine). Note that the segmentation is conducted directly in 3D even though the visualizations here are only in 2D.

2.3.2.2. Trainable Weka Segmentation

The Trainable Weka Segmentation (TWS) plugin from Fiji ImageJ is also applied to segment olivine and opx and independently constrain the mineral distribution. ImageJ is an open platform for scientific image analysis (Schindelin, J.; Rueden, C. T. & Hiner, M. C. et al., 2015). Fiji (Fiji Is Just ImageJ) is an open source package based on ImageJ (Schindelin, J.; Arganda-Carreras, I. & Frise, E. et al., 2012). TWS is a plugin in Fiji (Witten & Frank, 2005; Hall et al., 2009), which combines a collection of machine learning algorithms with a set of selected image features to produce pixel-based segmentations. For computers, features are quantities that can be calculated from an image. Many filtering algorithms are actually feature detectors. For instance, a low-pass filter can be regarded as a low-frequency signal detector. TWS includes a wide range of feature detectors, and the machine learning algorithm classifies each pixel based on the statistical correlation of their features. To segment the input image, TWS also requires a set of prior correctly classified pixels as the “learning material”. The set of labeled pixels is represented in the feature space and then used as the training set (i.e. “learning material”) for a selected classifier. [Figure 2.6](#) describes this pixel classification scheme in TWS.

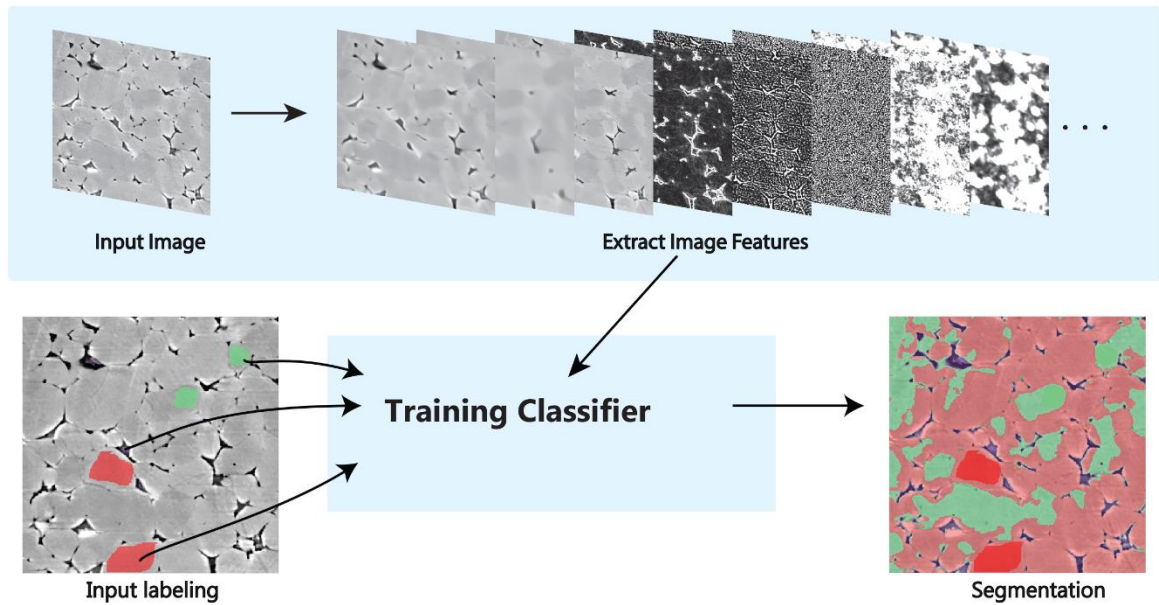
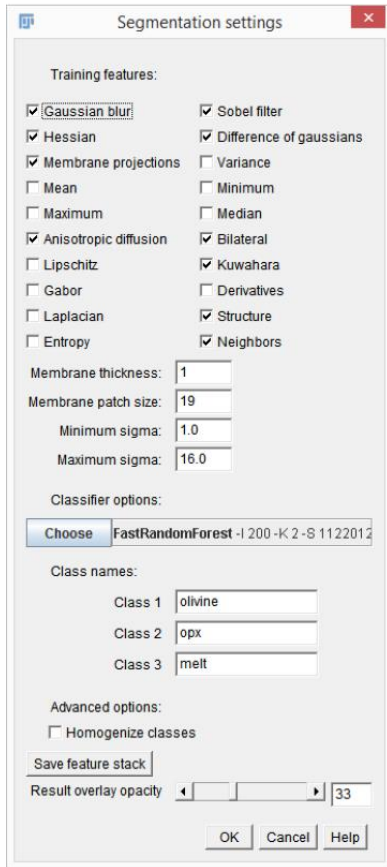


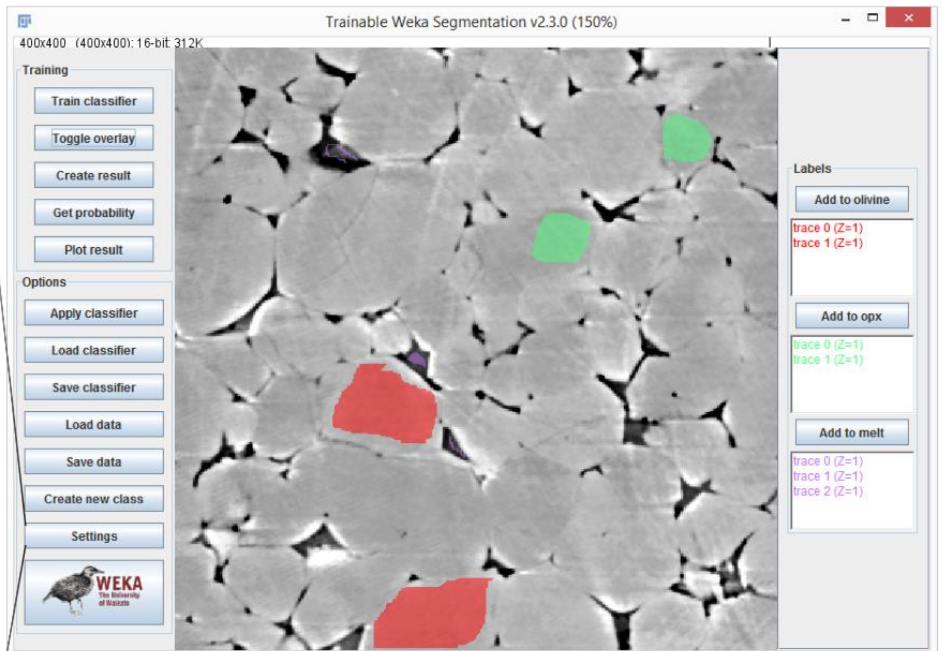
Figure 2.6 Schematic for TWS segmentation: Input labeling is represented in the feature space as a training set for the corresponding classifier. Then the classifiers are applied to the rest of the image/stack to obtain the overall segmentation.

The number of input labels determines the number of classes in the eventual segmentation result. In the partially molten harzburgite samples, there are three different phases (melt, olivine, opx), thus three input labels are required. The labeled areas are called traces. I use freehand selection tools in ImageJ to label areas of melt/opx/olivine as traces for each class (Figure 2.7 A). Generally, labeling more pixels as traces yields better segmentation results. As the 3D data set (image stack) in this study usually have more than 1000 slice, it is not efficient to label traces for every slice. I label at least two traces for each class every 100 to 200 slices (depending on the size of the subvolume) to limit the effect of background grayscale intensity variation. In the “Setting” panel, users can select the features for training the classifiers (Figure 2.7 B). Generally, the more features selected, the more sophisticated classifier would be expected but also the heavier the computation. Beside the five default features at the

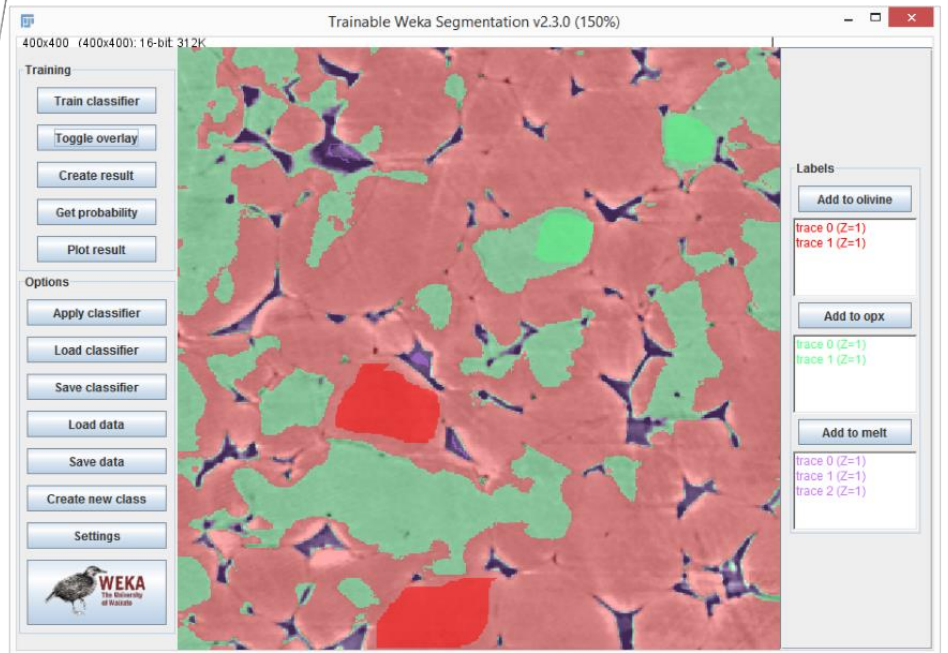
top, I also selected Bilateral, Anisotropic diffusion, Kuwahara, Structure and Neighbors as training features. The first three filters are all for edge-preserving noise reduction; Structure calculates the second-order partial derivative of the gray image and represents the edge information; Neighbors shifts the image in 8 different directions and calculates features of connectivity. Clicking on the “Train classifier” button will initiate the training and generate segmentation results ([Figure 2.7 C](#)). The segmentation results are saved as RGB tiff images. Note that the TWS also provides segmented melt phase, which can be used as an intended verification of the melt segmentation discussed in section 2.3.1.



B. Select training features



A. Label traces for each class



C. Segmentation results

Figure 2.7 Operations on TWS Panel in ImageJ: A. Manually label pixels to different classes (olivine, opx, melt) using the selection tool in ImageJ; B. In the Setting panel, select the features for the training set; C. Click “Train classifier” button to generate the segmentation results.

Chapter 3: Result of Melt and Mineral Distribution

Visual inspection of the reconstructed sample reveals significant melt fraction heterogeneity along the vertical direction of the partially molten harzburgite sample (Figure 3.1). The grayscale image on the left is a vertical cross section of a subvolume from sample hzb-15. The size of the subvolume is $400 \times 400 \times 1600$ voxels, which covers the majority of the vertical dimension of the sample core and is sufficiently wide to neglect the high-frequency local variations. The melt fraction of the 3-D subvolume is measured and plotted against depth, represented by slice number. Resolution, and therefore slice spacing, is $0.74 \mu\text{m}$. A moving average filter with a window length of 21 slices is applied to smooth the melt fraction profile. The melt fraction shows an increasing trend from the bottom to the top. Since the oxides and basalt powders were initially homogeneously mixed, this observed variation likely developed during the sintering phase and may have arisen from melt moving in the sample or by a reaction between the solid and melt phases that would have proceeded to different amount at different locations. The objectives of my thesis are to further document similar variations in our samples and to test several origins for these variations (see Discussion).

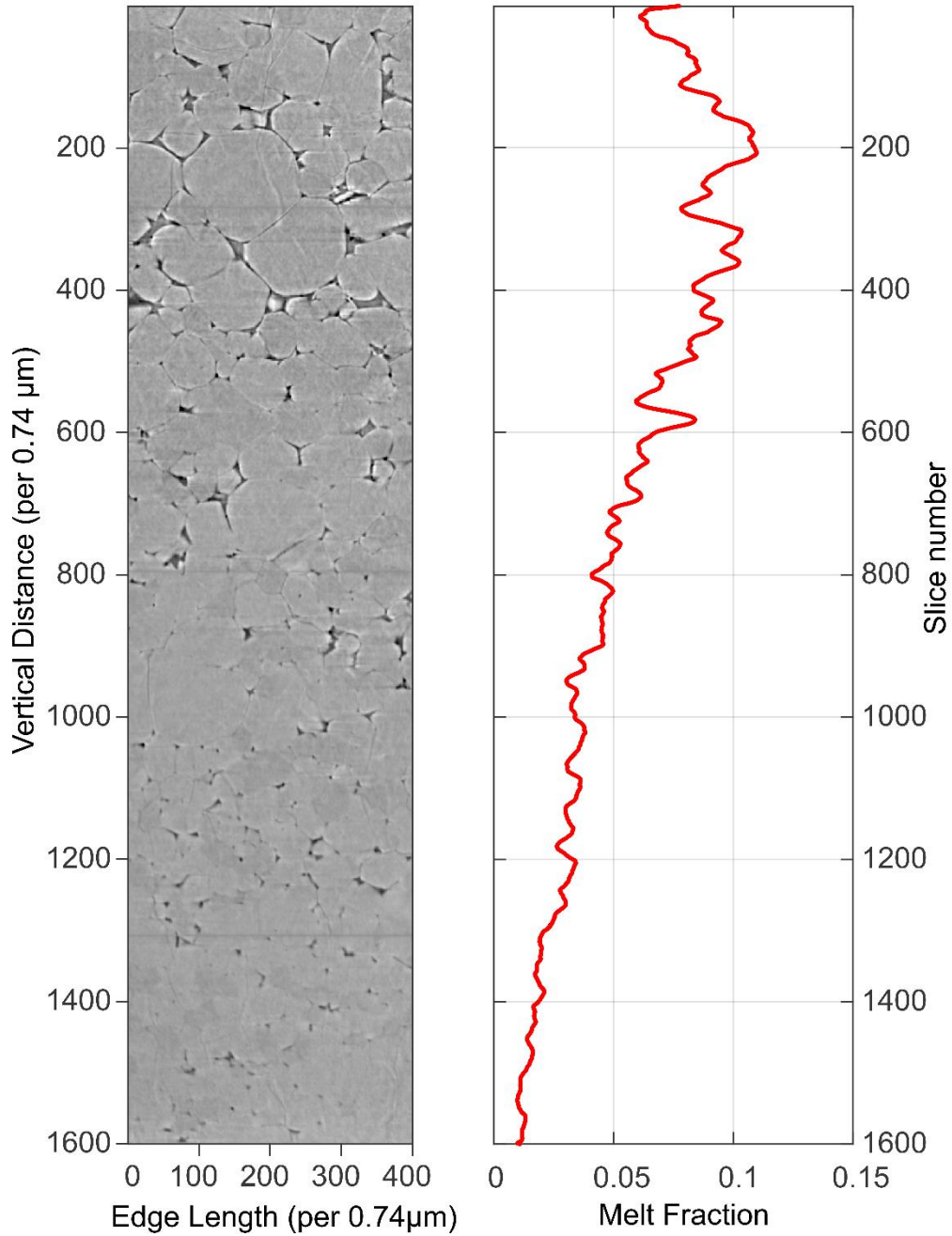


Figure 3.1: Vertical melt fraction heterogeneity. (Left) A cross section of a subvolume from sample hzb-15. The size of this subvolume is $400 \times 400 \times 1600$ voxels. The orientation of this image is the same as the orientation of the sample during sintering, i.e. the vertical direction. **(Right)** Measured melt fraction plotted against depth (measured in slices, where each slice is 0.74 micron thick). The melt fraction profile is smoothed using a moving average filter with a window length of 21 slices.

Two cores were drilled perpendicular to the axial axis of sintered samples so that the long axis of the sample is horizontal (Table 2). A similar analysis on these cores shows no systematic variation in the grayscale value (Figure 3.2). The high frequency variations might indicate a gradual grain size change in the subvolume. However, there is no evidence of a long wavelength trend in the horizontal melt fraction profile with the amplitude seen in the vertically cored samples. This indicates that the origin of the heterogeneity in the samples is linked to the vertical axis of the sample and implies either an influence of gravity or the architecture of the piston cylinder.

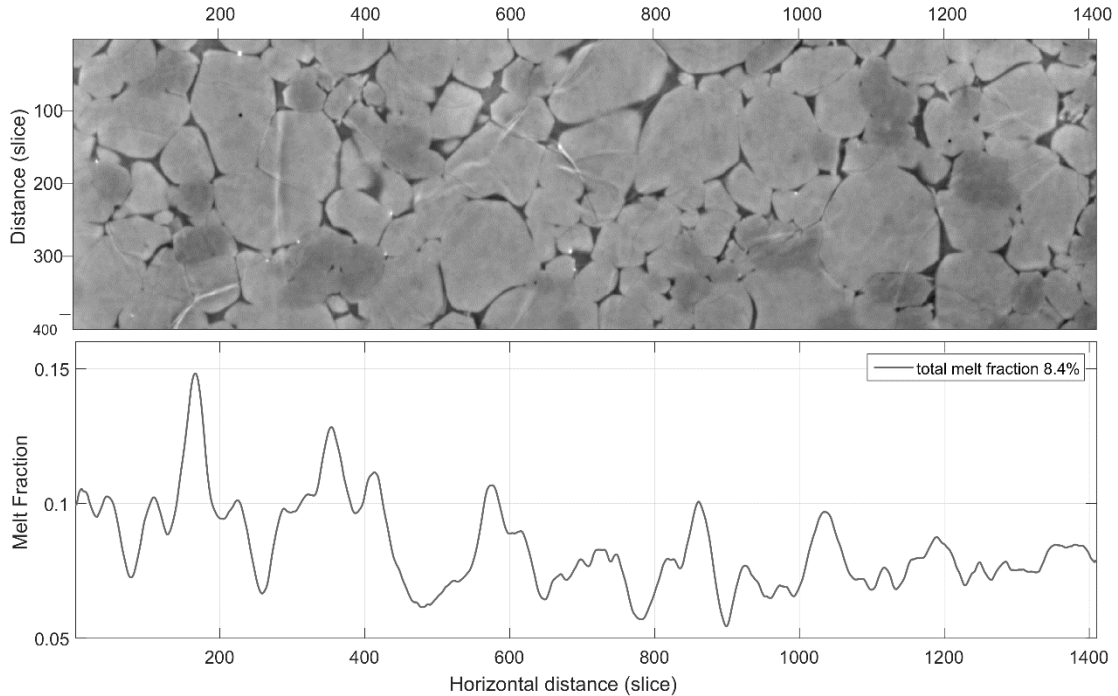


Figure 3.2: Horizontal variation in melt fraction in horizontally-cored sample hzb-2. Top: Grayscale image of a subvolume cropped of hzb-2. Bottom: Melt fraction plotted against horizontal distance along the axis of the sample core.

3.1 Vertical Melt Fraction

3.1.1 Time Series

Samples hzb-6 to hzb-10 were planned as a time series experiment. Starting with the same initial composition (5 volume % melt and an 82/18 olivine/pyroxene volume ratio), each sample remained at high temperature and pressure for a duration ranging from 42 to 336 hours (Table 2.1). This sample series can be used to constrain the amount of time needed for the melt heterogeneity to develop. Figure 3.3 shows the melt fraction profiles of subvolumes from this time series. The blue curves are the measured melt fraction profiles from the segmentation results. The thickness of the melt-grain boundary is smaller than the resolution of the pixelized images, thus pixels at the phase boundary, although considered as uniform, could actually be composed of different phases, which causes uncertainties on the melt fraction measurement. The lower bound or the upper bound of the melt fraction (shown in red and yellow) are obtained by shrinking or dilating the segmented melt phase by 1 pixel. Because these error bounds are obtained as a systematic modification of a given structure, the trend of the profiles is meaningful even if a straight line is often admissible within the error bounds. All of the profiles are smoothed using a moving average filter with a 21 slices window.

Samples with sintering duration shorter than 168 hours exhibit no significant long wavelength variation in the melt fraction with vertical position. However, hzb-9, the sample with 168 hours sintering duration (Figure 3.3 c) shows a significant upward increase in melt fraction, similar to hzb-15 (Figure 3.1). Sample hzb-10 (Figure 3.3 d) was sintered for a longer time but broke into pieces during unloading. Only the bottom

piece of hzb-10 was imaged. Although the imaged length is too short to capture vertical variations in melt fraction, such a variation may be inferred from the very low melt fraction detected in the core. Indeed, the melt fraction at the bottom of hzb-10 is much smaller than the nominal melt fraction. Thus it's reasonable to expect more melt in the upper part of the sample and consider hzb-10 as another piece of evidence for increasing melt fraction in the vertical direction. The time series suite shows that the melt fraction variation was not initially present in the sample and took 84 to 168 hours to develop, confirming that heterogeneity developed during sintering, when the sample was partially molten.

3.1.2 Regular Series

I also compared samples with similar sintering durations (168~200 hours) but with different nominal melt fractions (5%, 10% and 20%) or olivine/opx ratios (see [Figure 3.4](#)). I observed a systematic increasing trend in all those melt fraction profiles. Sample hzb-5 and hzb-14 have the same nominal melt fraction but different olivine/opx compositions and exhibit different increasing rates in melt fraction. Therefore the solid composition likely influences the development of melt fraction heterogeneities.

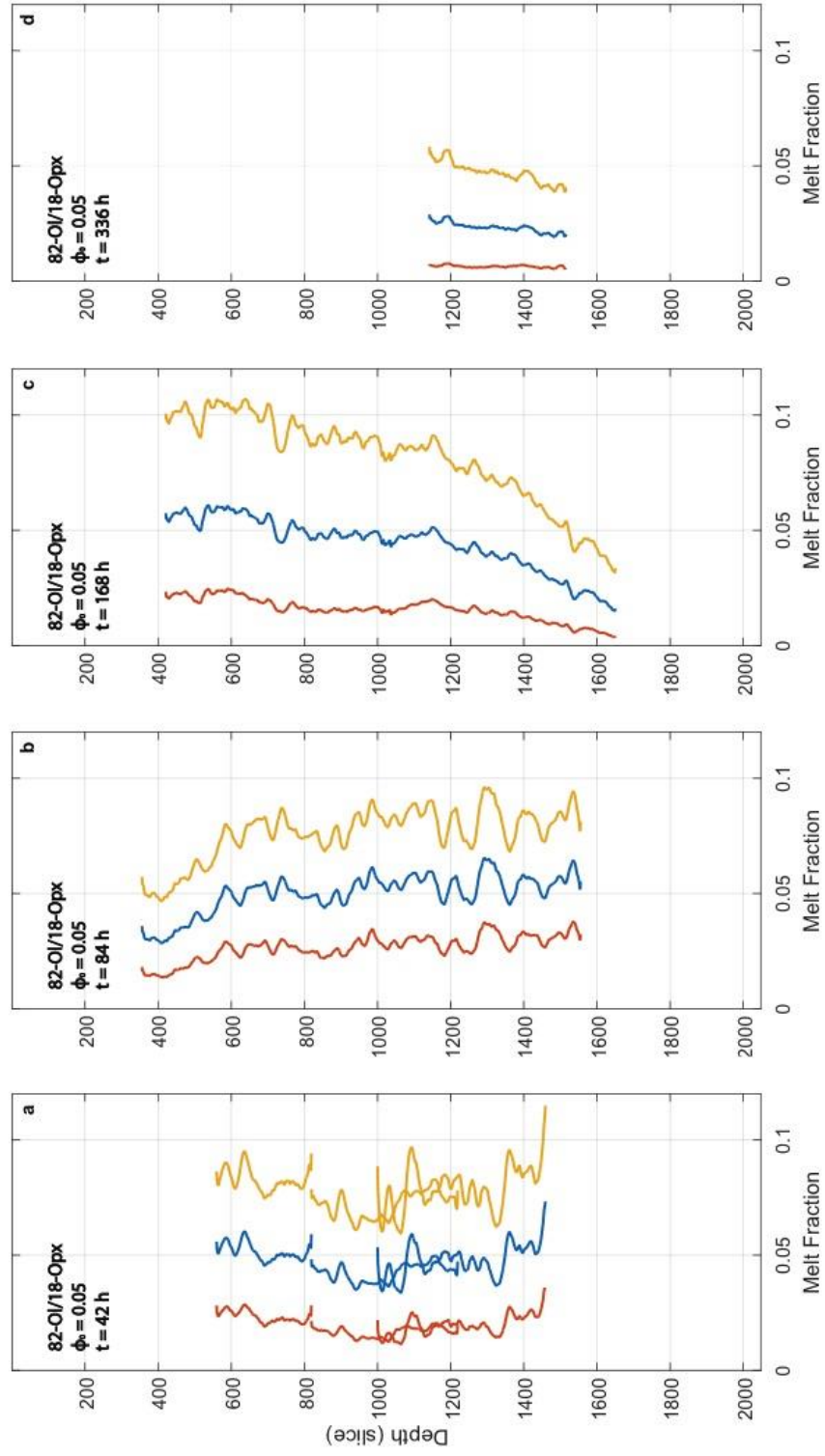


Figure 3.3: Vertical variation of melt fraction for sample hzb6-10. Each samples was sintered for different durations but started with the same 5 vol % nominal melt fraction and 82/18 olivine/opx ratio (table 1). a) sample hzb-6, sintered for 42 hours; b) sample hzb-7, sintered for 84 hours; c) sample hzb-9, sintered for 168 hours; d) sample hzb-10, sintered for 336 hours. The blue curves are the measured melt fraction profiles, while the red and yellow are the low bound and high bound given by the shrinking/dilating error estimation approach. The profiles from two subvolumes of sample hab-6 are reported

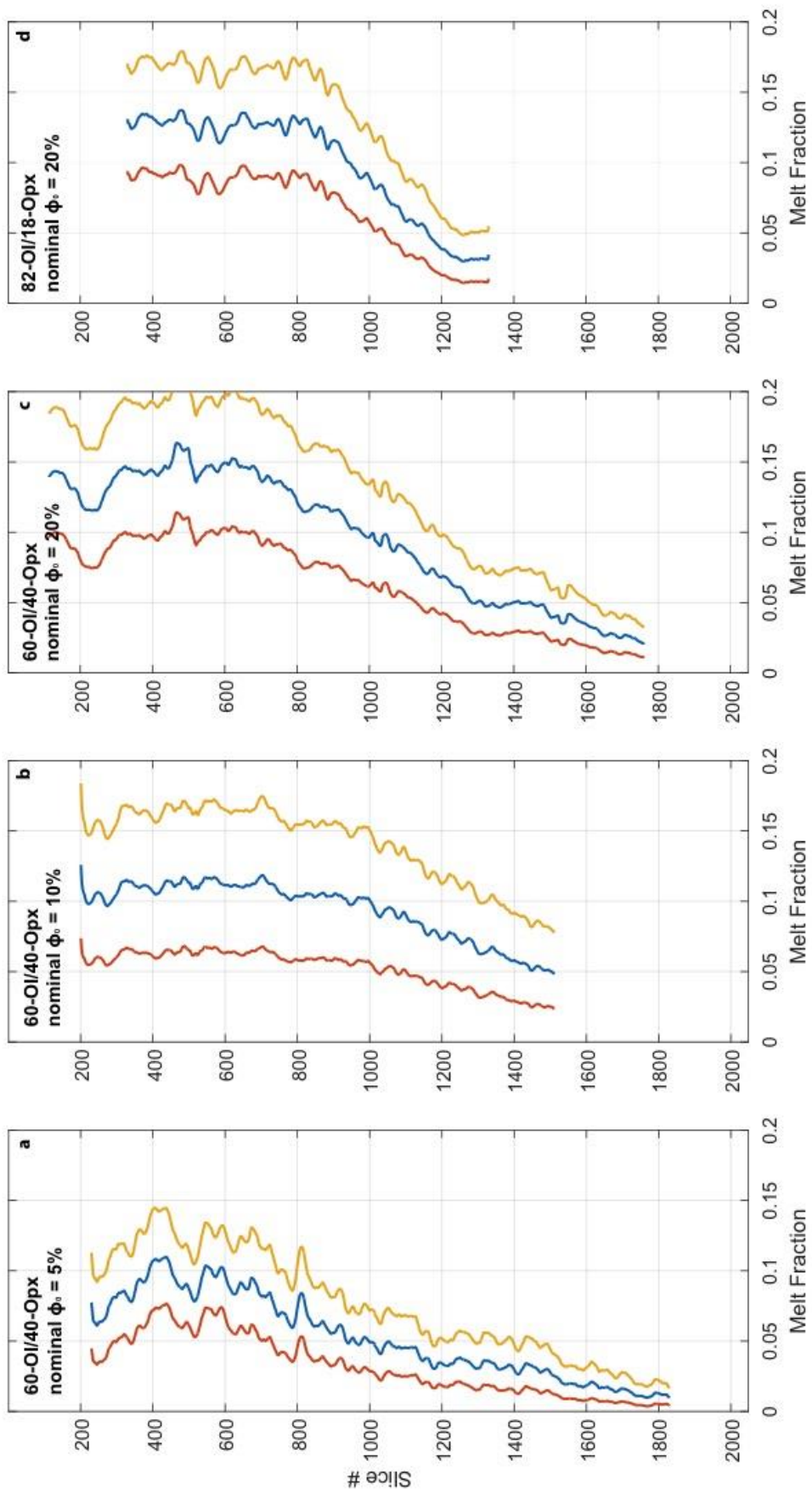


Figure 3.4: Vertical variation of melt fraction for samples with different nominal melt fractions or olivine/opx ratio. (a),(b),(c),(d) are subvolumes cropped from sample hzb-15, hzb-12, hzb-14 and hzb-5 respectively. The sintering duration of these samples are all between 168 hours to 200 hours. hzb-5 has a different starting olivine/opx composition. The legend is the same as in Figure 3.3.

3.2 Horizontal Melt Fraction

For each subvolume discussed above, I also calculated the melt fraction profiles along one horizontal direction and plotted the results in Figure 3.2 (see subvolume coordinates and all melt profiles in Appendix B). No significant trend is observed in the horizontal melt fraction variation, confirming the analysis result of horizontally-drilled samples.

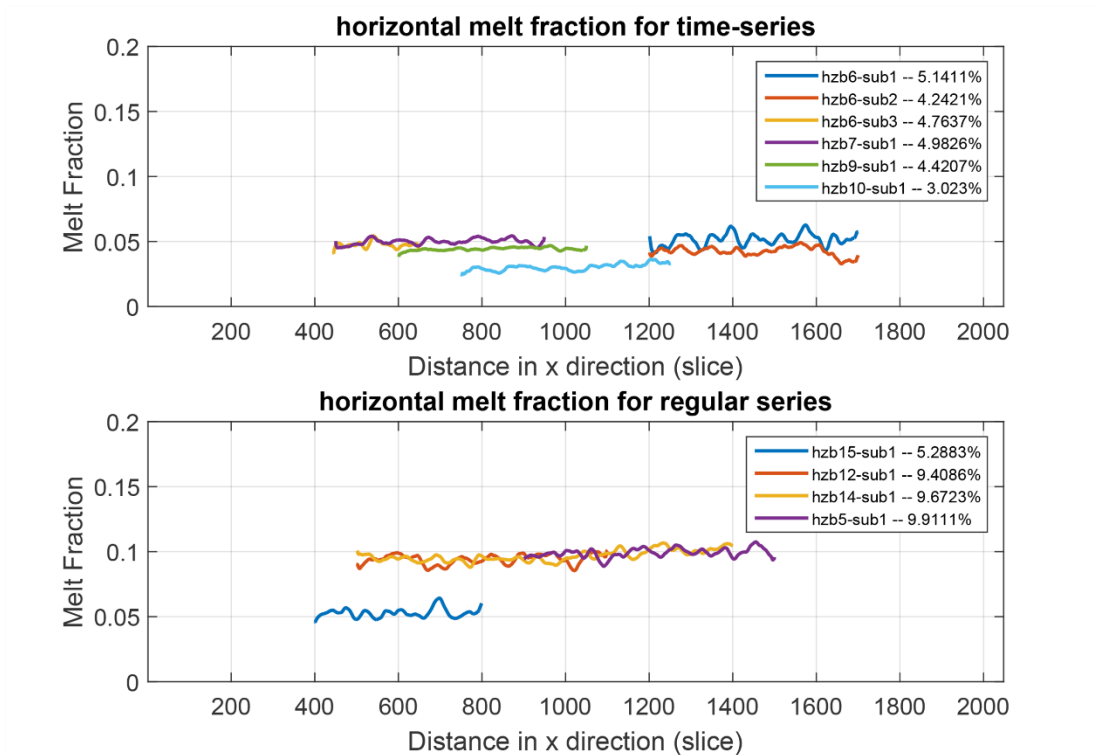


Figure 3.5: Horizontal melt variation for different sample subvolumes. Different colors represent different subvolumes. The upper panel shows the horizontal melt fraction variation of the time-series data; the lower panel shows the horizontal melt variation of the regular series data. The fraction in the legend is the total melt fraction in that subvolume.

3.3 Opx/Olivine Fraction

The opx/olivine volume fraction calculated from the two segmentation algorithms are plotted together with the melt fraction. Figure 3.6 – Figure 3.9 show the

mineral volume fraction of the time-series data. [Figure 3.10](#) – [Figure 3.14](#) shows the mineral volume fraction of the regular series samples. The mineral fraction variation is also calculated for the horizontally cored sample ([Figure 3.13](#)).

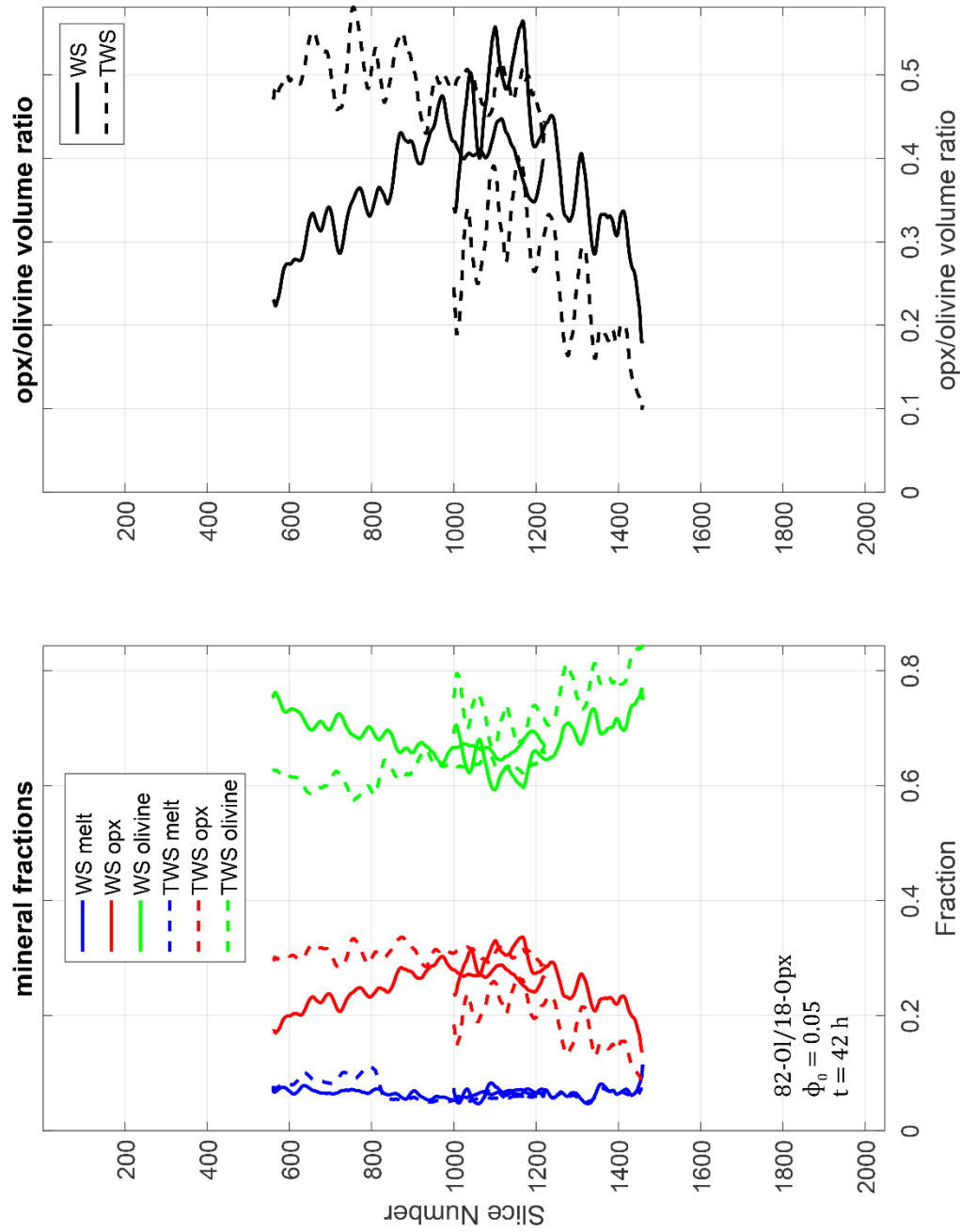


Figure 3.6: Melt and mineral volume fraction along hzb-6 sample core axis. In the left panel, blue, red and green curves represent the volume fraction of melt, opx and olivine. In the right panel, the black curve represents the opx/olivine volumetric ratio along the core axis. In both panels, the solid curves are calculated from Avizo[®] segmentation results and dashed ones from TWS. The curves are not continuous because they are the combination of two subvolumes. The sintering duration for hzb-6 was 42 hours.

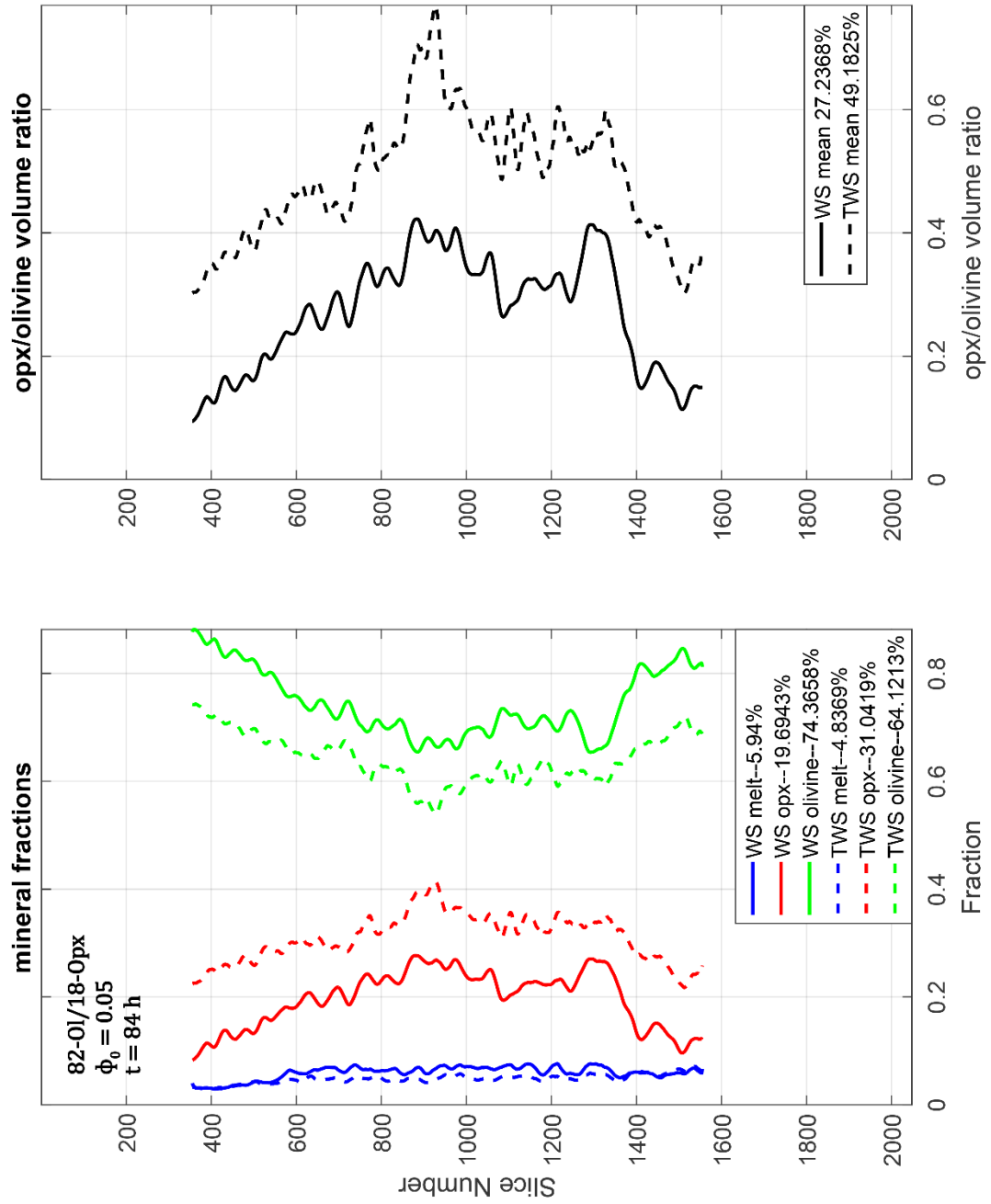


Figure 3.7: Melt and mineral volume fraction along hzb-7 sample core axis. The sintering duration for sample hzb-7 was 82 hours.

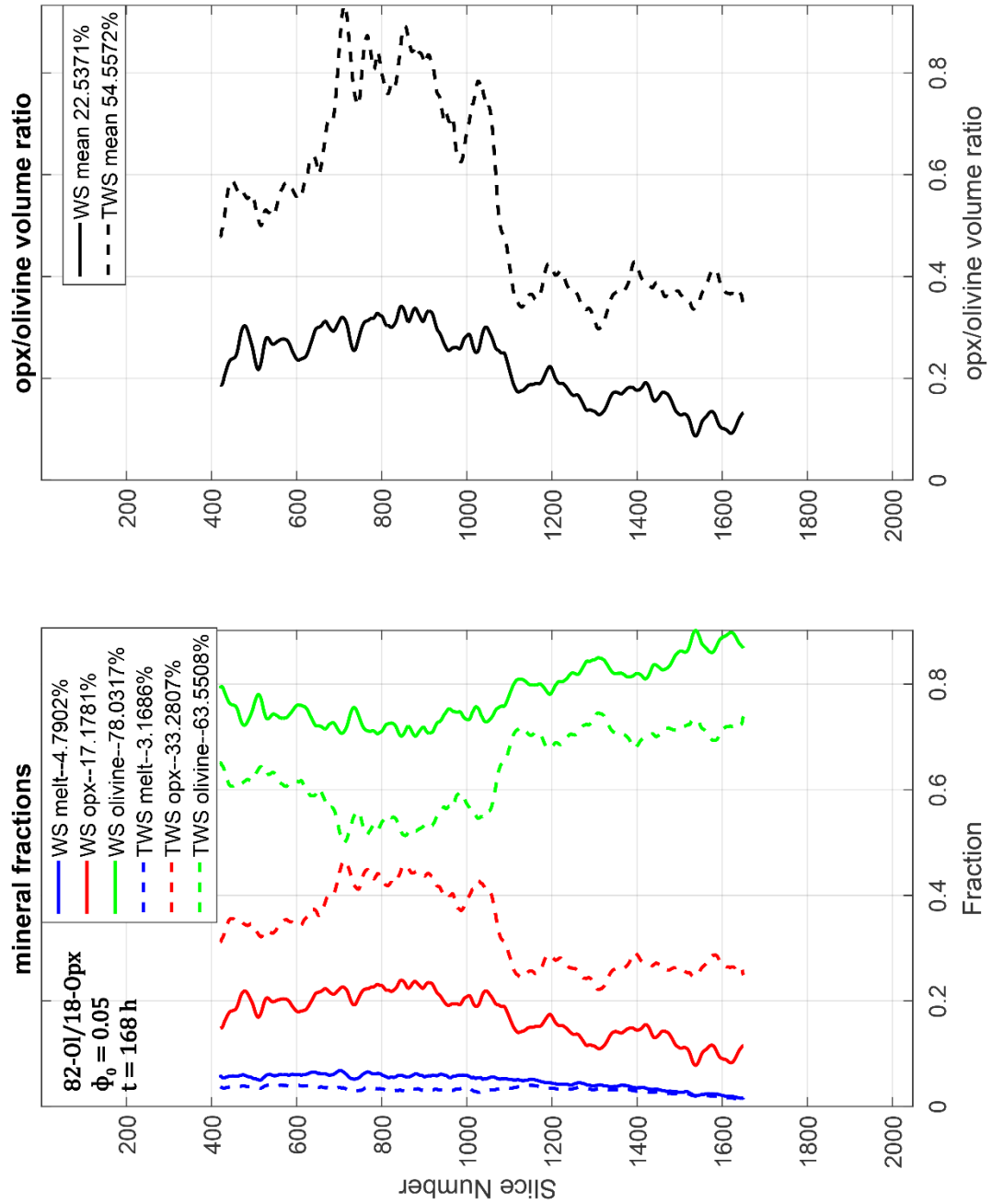


Figure 3.8: Melt and mineral volume fraction along hzb-9 sample core axis. The sintering duration for sample hzb-9 was 168 hours.

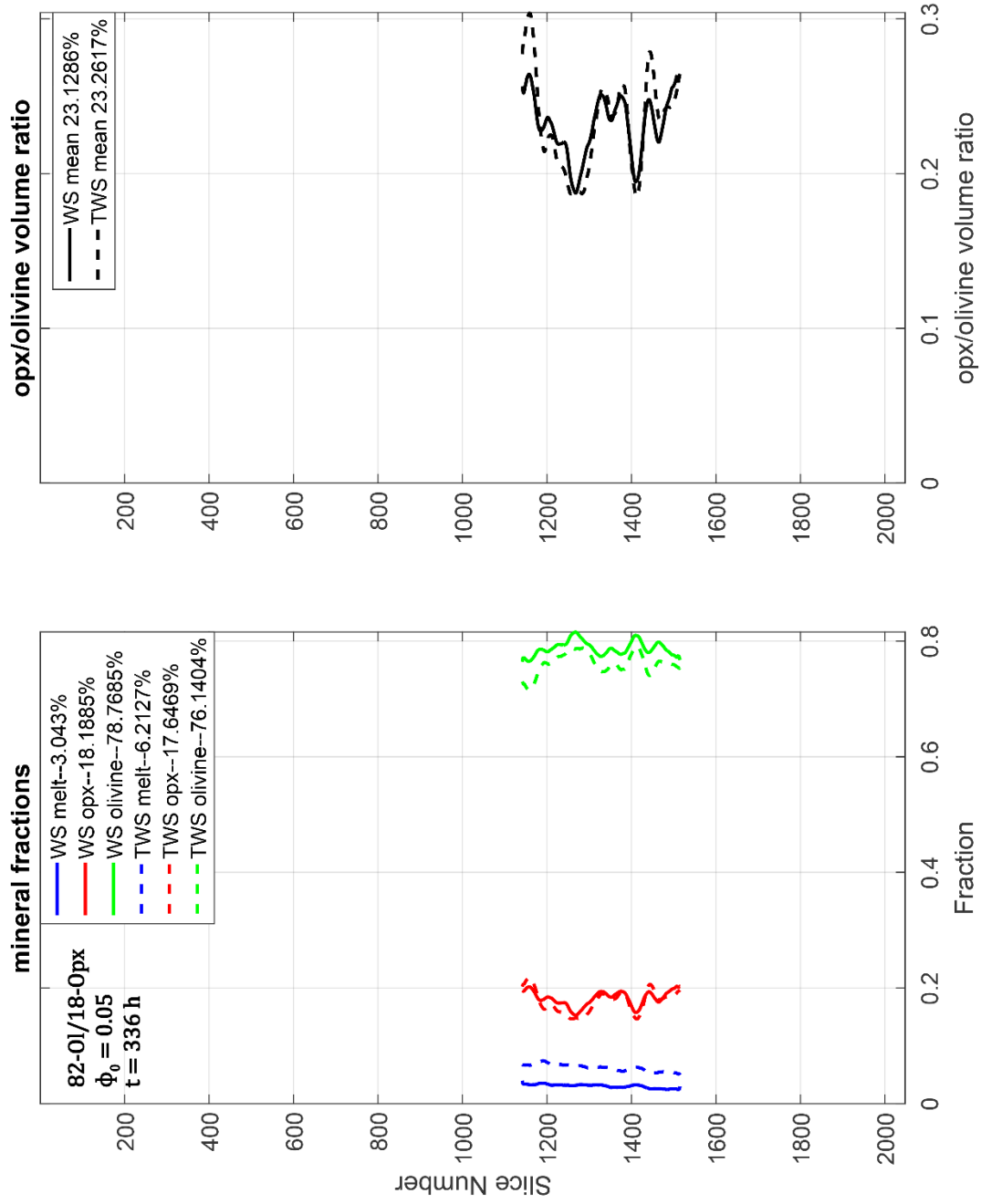


Figure 3.9: Melt and mineral volume fraction along hzb-10 sample core axis. The sintering duration for sample hzb-10 was 336 hours. Sample hzb-10 broke during the unloading, and only the bottom piece was imaged and studied.

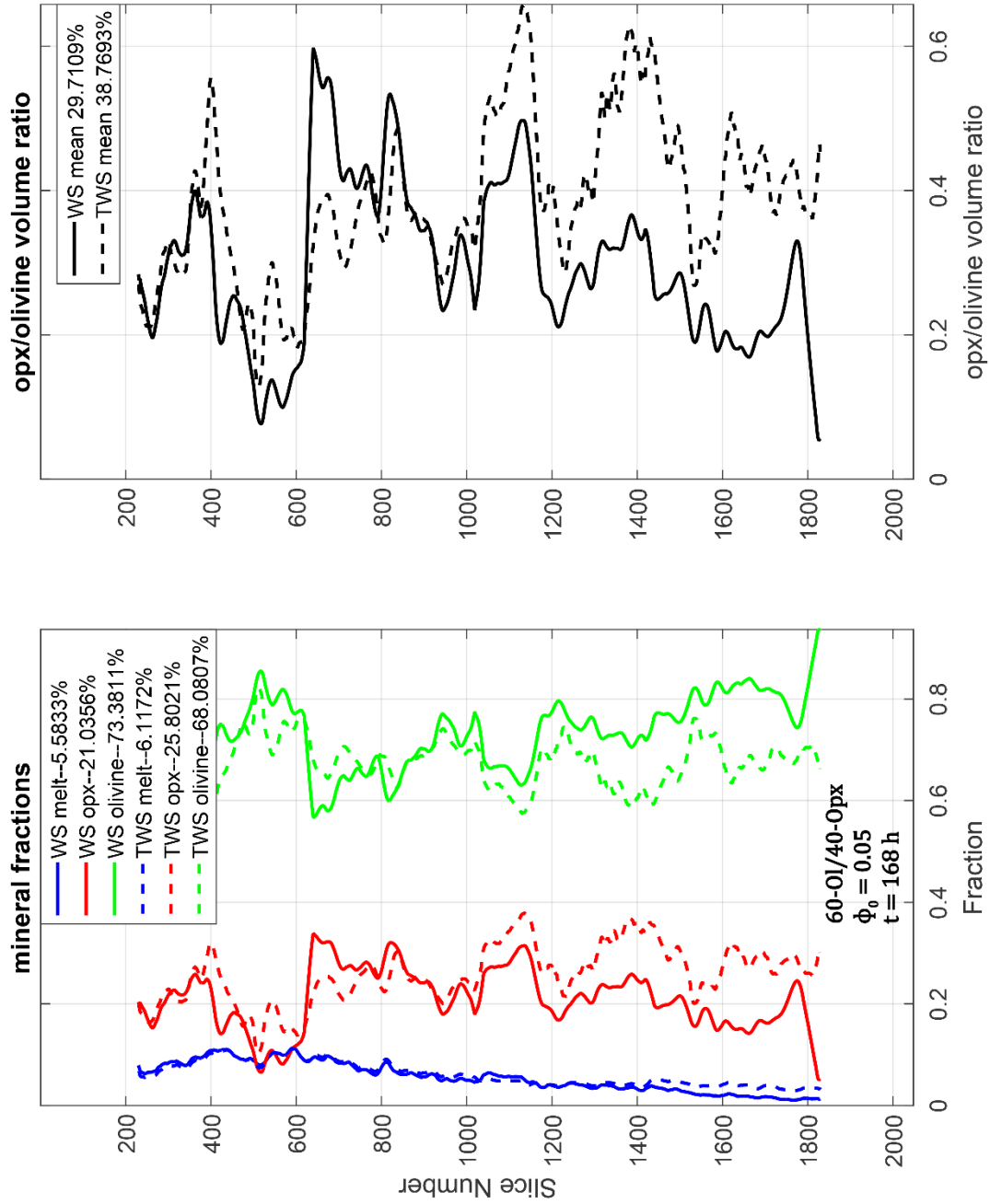


Figure 3.10: Melt and mineral volume fraction along hzb-15 sample core axis. Sample hzb-15 has a nominal melt fraction of 0.05 and starting olivine/opx = 60/40; it was sintered for 168 hours. The watershed-segmented curves have several sharp changes in opx/olivine fraction because the subvolume was further divided into 4 smaller subvolumes to limit the effect of background grayscale intensity variation.

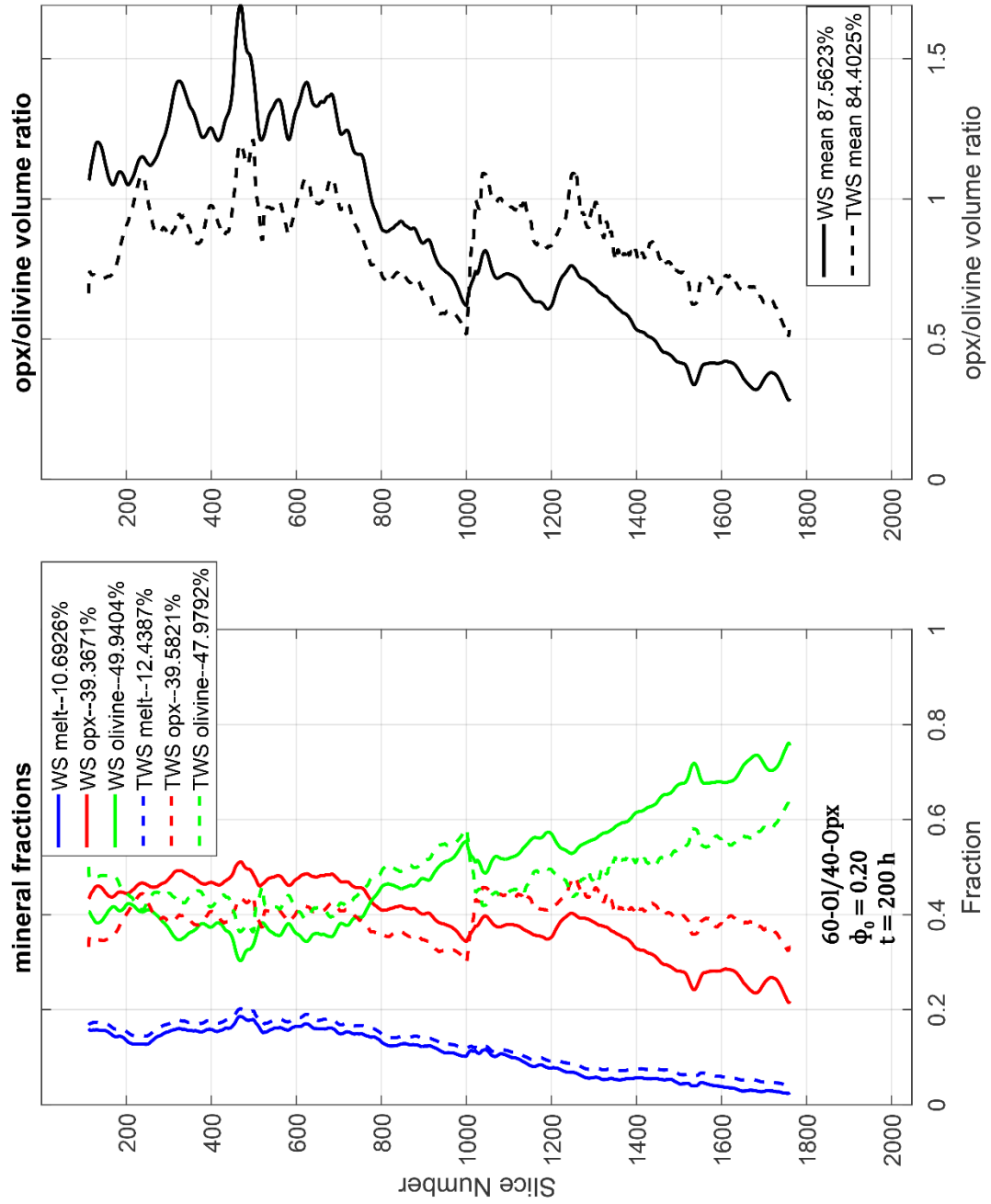


Figure 3.11: Melt and mineral volume fraction along hzb-14 sample core axis. Sample hzb-14 has a nominal melt fraction of 0.20 and starting olivine/opx = 60/40; it was sintered for 200 hours.

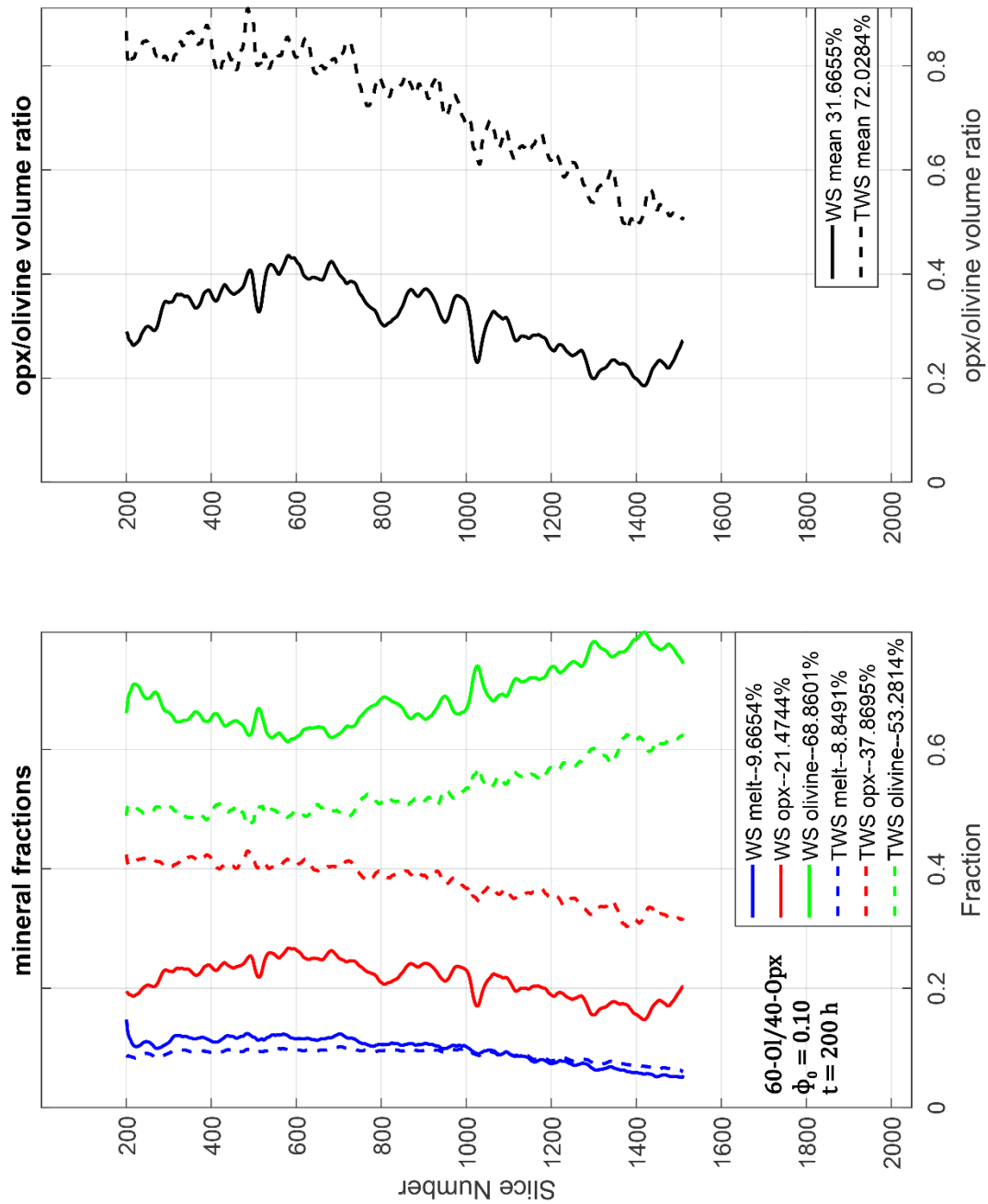


Figure 3.12: Melt and mineral volume fraction along hzb-12 sample core axis. Sample hzb-12 has a nominal melt fraction of 0.10 and starting olivine/opx = 60/40; it was sintered for 200 hours.

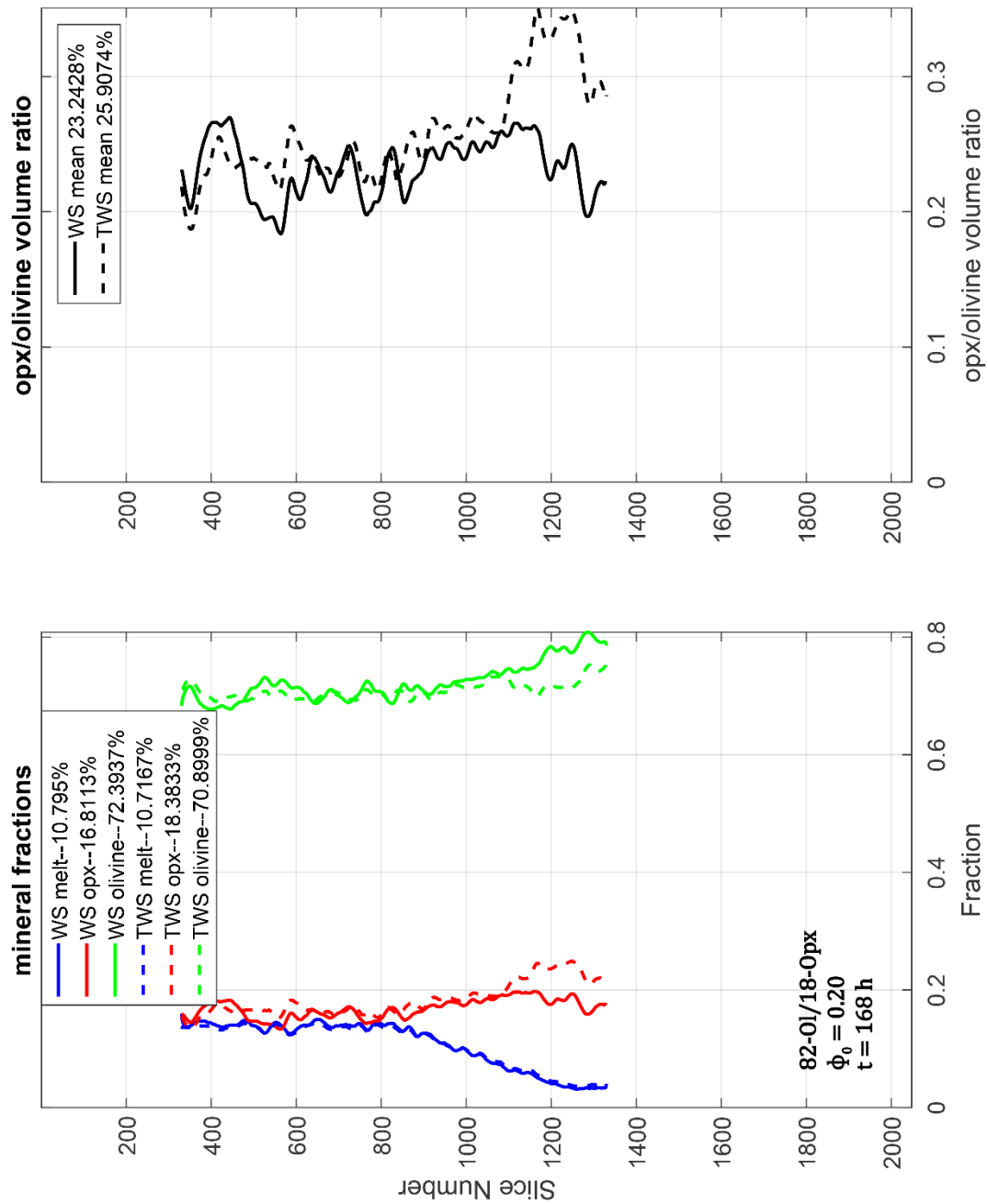


Figure 3.12: Melt and mineral volume fraction along hzb-5 sample core axis. Sample hzb-5 has a nominal melt fraction of 0.20 and starting olivine/opx = 82/18; it was sintered for 168 hours.

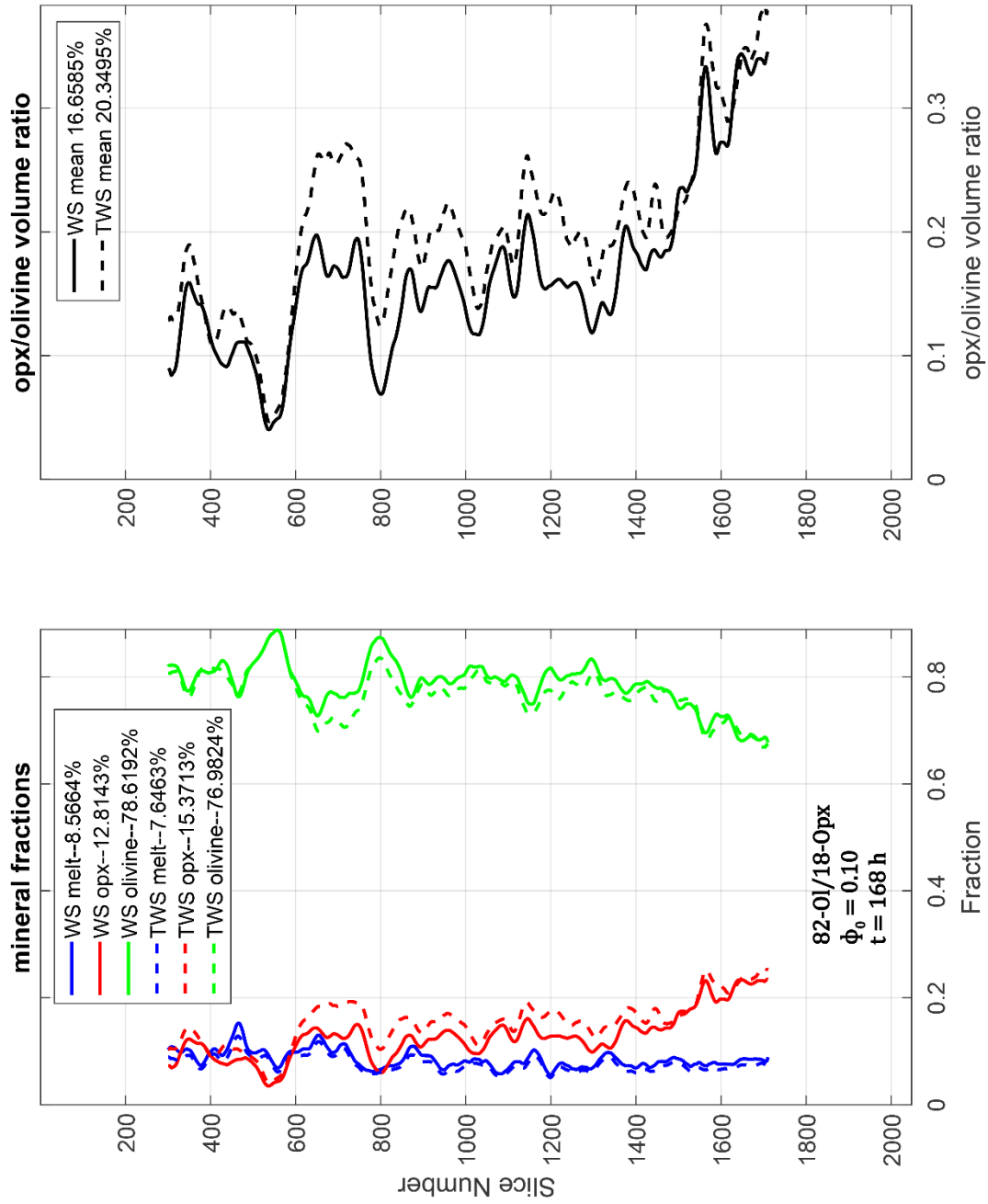


Figure 3.13: Melt and mineral volume fraction along hzb-2 sample core axis. Sample hzb-2 has a nominal melt fraction of 0.10 and starting olivine/opx = 82/18; it was sintered for 168 hours. After the sintering and quenching, sample hzb-2 was horizontally cored. The mineral fraction profiles in this figure are plotted along the core axis, i.e. the horizontal direction.

Chapter 4: Discussion

The melt heterogeneities observed in the samples developed during sintering, while the sample was partially molten. Identifying the origin of these heterogeneities is important to determine whether they might develop in natural settings and possibly contribute to the generation or stabilization of the melt channels inferred to increase the efficiency of melt segregation at mid-ocean ridges. Here I discuss several possible origins of the melt heterogeneities, which includes considerations on gravity-driven compaction, surface energy minimization, and thermal migration.

4.1 Buoyancy-Driven Melt Migration

The first mechanism that may be proposed as the origin of the observed heterogeneities is buoyancy-driven flow. The melt is more buoyant than solid harzburgite and therefore may be expected to migrate upward under the action of gravity and segregate near the top of the sample. McKenzie (1984), among others, presents a solution to the buoyancy-driven compaction of a two-phase column (Appendix A). However, the duration of the experiments and the length of the sample imply that buoyancy alone cannot generate the observed heterogeneities.

First, the size of the samples is too small for a compaction profile to be observed. As mentioned in section 1.2, changes in pressure can only be sustained over length scales less than the compaction length (Eq. 3). Shear viscosity of the solid matrix can be estimated from previous shear experiments on partially molten olivine and

MORB aggregates. Holtzman et al. (2003) gave a shear viscosity of $2.19 \times 10^{12} \text{ Pa} \cdot \text{s}$ at a strain rate of $4.6 \times 10^{-4} \text{ s}^{-1}$. In our experiment, the total deformation of the sample during the hot press was about 0.5, thus the strain rate is about $0.5/100 \text{ hour}^{-1} \sim 1.4 \times 10^{-6} \text{ s}^{-1}$. Using the power law relationship between the stress and the strain rate $\sigma = A \cdot \dot{\epsilon}^n$ with $A =$ a constant and $n = 3$, I estimated the shear viscosity η for our sample to be $1 \times 10^{14} \text{ Pa} \cdot \text{s}$. Digital rock physics experiments determine the permeability of partially molten olivine and basalt aggregates ranging from 2×10^{-16} to $5 \times 10^{-13} \text{ m}^2$ for nominal melt fraction of 0.02 to 0.20 (Miller et al., 2014). Taking $2 \times 10^{-16} \text{ m}^2$ as the minimum permeability of our samples, $\eta=10^{14} \text{ Pa} \cdot \text{s}$ as the scale of the shear viscosity of the matrix (sample under hydrostatic pressure), and $\mu = 10 \text{ Pa} \cdot \text{s}$ as the melt viscosity results in a compaction length at least of 0.01 m., which is an order magnitude larger than our sample length ($\sim 1 \text{ mm}$). The bulk viscosity ζ can only increase the compaction length. Thus it is unlikely that our samples feature a compaction or decompaction boundary.

Second, melt migration in the sample is too slow to have significant effects over the duration of our experiments. Darcy's law (Eq. 2) gives the relative velocity of melt penetrating the matrix. The pressure gradient is estimated as $\Delta\rho g \sim 3000 \text{ N/m}^3$. Using the constitutive relation from Miller et al. (2014) $K = \phi^{2.6} d^2 / C$ with the average grain size $d = 35 \mu\text{m}$ and the geometry parameter $C = 58$, a partially molten system with a porosity of $\phi=0.05$ will have a permeability of $8 \times 10^{-15} \text{ m}^2$. From Eq.(3), the melt velocity is estimated to be only $5 \times 10^{-11} \text{ m/s}$. Over 300 hours, melt is expected to travel only $\sim 50 \mu\text{m}$ under the influence of gravity much smaller than our observed scale of melt distribution heterogeneity. Thus buoyancy alone is unlikely to generate the

significant and systematic melt fraction heterogeneities observed in our sample over such experimental durations.

4.2 Surface Tension Driven Melt Migration

Forces other than buoyancy can drive melt migration in a two-phase aggregate. For example, Stevenson (1986) pointed out that the pressure difference between two phases caused by surface tension could redistribute the melt in the partially molten media. The surface tension pressure difference is given by the Young-Laplace equation:

$$P_s - P_l = \Delta P_\sigma = \frac{\gamma_{sl}}{r} \quad (9)$$

where P_s and P_l are the solid pressure and liquid pressure respectively, γ_{sl} is the solid-liquid interfacial energy, and r is the radius of curvature of the interface (Figure 1.2). Bercovici et al. (2001) derived a new set of governing equations of the two-phase problem that includes explicitly the effects of surface tension, using the averaging approach (see Drew, 1971; Drew & Segel, 1971). In their model, the interface area density α (interface area per unit volume) is assumed as a function of the porosity ϕ wherein $d\alpha/d\phi$ is the summation of the average interface curvatures. The surface energy density is given by $\gamma\alpha_0$, where α_0 is the average interface area density estimated as $\sim 10^6 \text{ m}^{-1}$ for micron-sized pores and grains and γ is the interfacial energy at olivine-basalt interface, evaluated at $\sim 1 \text{ J} \cdot \text{m}^{-2}$ (Cooper & Kohlstedt, 1982). Bercovici et al. (2001) compare the importance of surface tension vs. buoyancy over a length scale R using the dimensionless number $\gamma\alpha_0/(\Delta\rho gR)$. At the scale of our samples, $R \sim 1 \text{ mm}$

and this ratio is $\sim 10^5$. Therefore, surface tension is much more efficient than buoyancy at moving melt at length scale of our samples. Darcy's law implies that melt might move 10 mm over the duration of our experiments. However, to generate the observed vertical melt fraction variation by surface tension, there has to be a vertical variation in the interfacial energy γ . The interfacial energy varies with temperature, and we discuss the effect of temperature below.

The Eötvös rule empirically predicts the surface energy γ of an arbitrary liquid substance as a linearly decreasing function of temperature (e.g. Woodbury, 1997).

$$\gamma = \gamma_0 \left(1 - \frac{T}{T_c}\right) \quad (10)$$

where T is temperature, T_c is a constant that represents the critical temperature of the liquid, γ_0 is a constant that represents the surface tension at zero temperature.

In all the experiment runs, the sintering temperature was controlled in the graphite furnace, but temperature variations of a few degrees along the sample chamber could be possible. If the temperatures at the top and the bottom of the sample chamber are T_1 and T_2 respectively, there could be a 10°C difference between T_1 and T_2 . I assume the solid pressure P_s and the radius of curvature r as constant. Then the fluid pressure P_l can be expressed as a function of T :

$$P_l = P_s - \frac{\gamma_0}{r} \left(1 - \frac{T}{T_c}\right) \quad (11)$$

So the pressure gradient generated by surface tension fluid pressure is:

$$\nabla P_l = \frac{\gamma_0}{r T_c} \nabla T = \frac{\gamma_0}{r T_c} \frac{T_1 - T_2}{R} \quad (12)$$

We use an $R \sim 1$ mm as the sample length, $r \sim 50$ μm (grain size) approximately as the average radius of curvature, and $\gamma_0/T_c \sim 0.0003$ J/m^3 (Frolov and Mishin, 2009) to estimate the fluid pressure gradient. Using these numbers and Eq.12, we can estimate the surface tension pressure gradient in fluid ∇P_l to be $\sim 6 \times 10^4$ Pa/m . Similar to the melt velocity analysis in 4.1, the surface tension pressure gradient could generate a melt velocity of $\sim 10^{-11}$ m/s and a melt migration distance of 0.01 mm (in 300 hours), which is two magnitude smaller than the observed scale. Thus, the small temperature variation can't provide enough gradient in surface tension to generate the observed melt profile.

4.3 Lithologic Partitioning

Mineral composition is another factor that affects the solid-liquid interfacial energy γ_{sl} and thus the dihedral angle at the solid-liquid interface. The phenomenon that local melt abundance varies with the spatial mineralogy change is referred to as lithologic partitioning. When textural equilibrium is reached, the total free energy in the system should reach its minimum. [Figure 4.1](#) illustrates the total surface energy in a system as a function of melt fraction at different dihedral angles (i.e. different mineral compositions). For each given dihedral angle, there is a unique melt fraction that minimizes the total surface energy of the system. If an open system initially has a uniform melt fraction (as the dashed line shows), the system will either absorb or expel melt to minimize the surface energy. The lithological melt partitioning has been modelled by Park and Yoon (1985) and observed in quartz/water assemblages (Watson 1999). The mechanism of the fluid redistribution is proposed to involve both chemical

reactions and physical diffusion, and known as the reaction infiltration instability (RII). The melt fraction is adjusted to minimize system energy by dissolving grains at the low melt region, precipitating at high melt region and melt redistribution through diffusion (Watson, 1999).

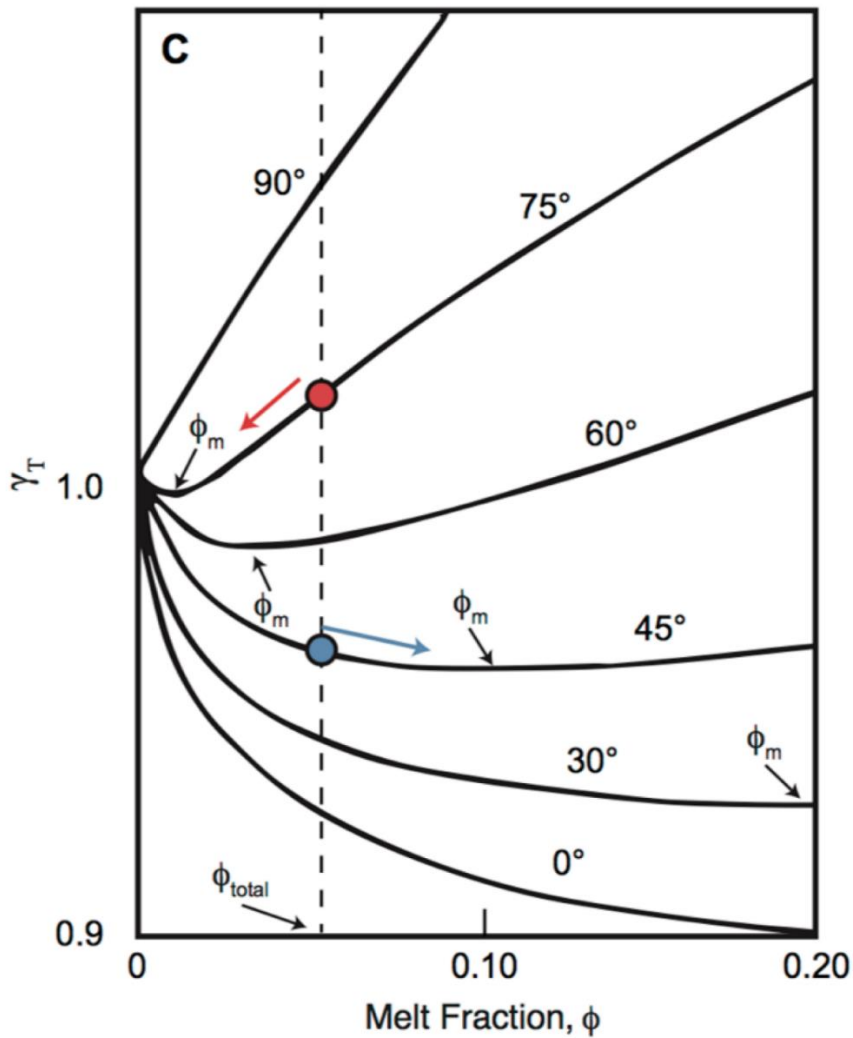


Figure 4.1: Schematic figure of minimum energy melt fractions for a system with melt and different minerals. The total surface energy of a melt-grain system is normalized by that of a melt-free system and plotted against the melt fraction for different given dihedral angles. The black dashed line shows an initial melt fraction in a system that is identical for each phase, and arrows show the direction in which the melt content moves in order to reach the minimum surface energy. The red dot and blue dot represents melt-opx system and melt-olivine system, respectively. From Miller et al. (2016).

Miller et al. (2016) observed that in partially molten harzburgite, olivine-rich regions tends to have higher melt fractions compared to opx-rich regions. They concluded that lithological partitioning is responsible for the melt redistribution at micrometer scale. In this study, the vertical variations in olivine to opx fraction is quantified in the sample subvolumes shown in Section 3.3. Except hzb5, which shows a negative correlation between the melt fraction and opx/olivine volume ratio, no other samples exhibit systematic variation of opx/olivine ratio along the vertical axis. This suggests that lithologic partitioning does not play a significant role in melt redistribution at millimeter scale.

4.4 Thermal Migration

Temperature gradient could significantly affect crystal compaction and melt segregation during magma crystallization through two different diffusion potentials (Walker et al., 1982; Leshner, 1986; Leshner & Walker, 1986; Leshner & Walker, 1988). The first diffusion potential arises from the mineral concentration gradient caused by the temperature-dependent variations of mineral solubility (also referred to as saturation gradient chemical diffusion). The second diffusion potential results directly from the temperature gradient in the melt (the Soret effect). Leshner & Walker (1988) collectively referred to the temperature gradient driven consolidation as thermal migration and proved its existence in silicate magma crystallization.

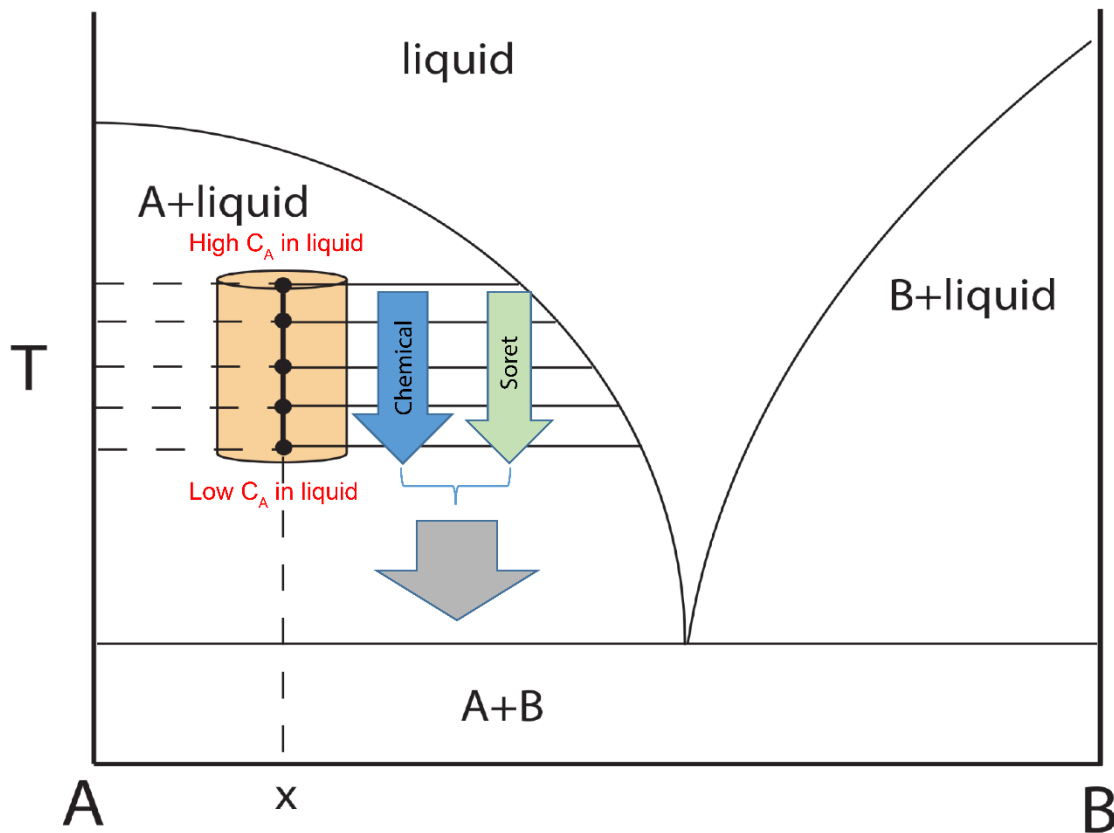


Figure 4.2: Schematic phase diagram illustration for saturation gradient chemical diffusion and Soret diffusion. A binary system with an initial composition x is placed in a temperature gradient under the liquidus (sample is shown in orange). The system quickly establishes a local saturation equilibrium along the T gradient causing chemical diffusions as subsequences of the concentration gradient for A and B. Blue arrow shows the direction of saturation gradient chemical diffusion of component A. Soret diffusion is caused by the irreversible heat flow in the liquid and can either assist the chemical diffusion (as shown in this figure) or impede or even change the direction of the diffusion.

Figure 4.2 illustrates the saturation gradient chemical diffusion and Soret diffusion in a binary system composed of components A and B ((Leshner and Walker, 1998). The system has an initial composition x , is open to heat and isolated from external mass exchange. Once the system is placed in a temperature gradient under the liquidus, it will quickly establish a local saturation equilibrium along the temperature gradient. High temperature region dissolves more A, thus the liquid at the hot end will

have a higher C_A (concentration of A) and consequently a lower C_B (concentration of B). The concentration gradient in the liquid will drive A to diffuse from the hot end to the cold end and B vice versa. As more component A diffuses the cold end, the cold end gets saturated with A and starts to precipitate A to maintain the saturation concentration in the liquid. This process is called saturation gradient chemical diffusion. Due to the irreversible flow of heat along the temperature gradient, the liquid itself could undergo spontaneous internal diffusion, which is called Soret diffusion. Under a temperature gradient, a component of the saturating phase may tend to diffuse toward either the warmer region or colder region driven by Soret effect. Thus, the Soret diffusion could either assist the saturation gradient chemical diffusion or impede that process. In this manner, phase A and B can be redistributed along the temperature gradient by liquid state diffusion. With time, phase A can completely dissolve at the hot end and the liquid will be completely eliminated from the cold end. To apply this model to our samples, olivine or opx, which experience partially melting, can be considered as phase A and minerals in basalt, which totally melts during the sintering, can be considered as phase B.

Leshner & Walker (1988) have shown rapid olivine compaction and silicate melt expulsion due to thermal migration at a relatively small thermal gradient (i.e., $\sim 28^\circ\text{C}/\text{mm}$) at high temperature (1620°C) and high pressure (0.7 GPa). Huang et al. (2008) also observed melt segregation by thermal migration in partially molten wet andesite. In both studies, the liquid phase (melt) diffuses from the cold region to the hot region. The solute flux by thermal migration is expressed by (Leshner and Walker, 1988):

$$J = -Ddc/dz - D'cdT/dz \quad (13)$$

where J the flux of a certain solute (in moles per unit area per unit time); c is the molar concentration of the solute; T is temperature; z is the spatial coordinate; D is the chemical diffusivity of the solute and D' is the thermal diffusivity. The first term on the right hand side of Eq. (13) is the solute flux along the concentration gradient driven by saturation conditions and the second term is the flux component that are driven by temperature gradient alone, i.e. Soret diffusion. Following Lesher and Walker (1988) the melt migration velocity can be estimated by:

$$v_c = D \left[\left(\frac{dx}{dT} \right)_{liq} + S_T x \right] dT/dz \quad (14)$$

where v_c is the compaction rate in Lesher & Walker (1988) and equivalently considered as the melt migration velocity here; x is the concentration in mole fraction and $(dx/dT)_{liq}$ is the inverse slope of the relative liquidus; $S_T = D'/D$ is the Soret coefficient. Previous studies suggest that S_T is of the order $10^{-3} \text{ } ^\circ\text{C}^{-1}$ for a wide variety of materials including mafic magma compositions (Lesher & Walker, 1986), sea salt (Caldwell & Eide, 1985) and also organic materials (Platten et al., 2003 etc.). Using $D = 1 \times 10^{-6} \text{ cm}^2/\text{s}$ and $(dx/dT)_{liq} = 1 \times 10^{-3} \text{ } ^\circ\text{C}^{-1}$ from Lesher & Walker (1988), at a temperature gradient of $10 \text{ } ^\circ\text{C}/\text{mm}$, I estimated $v_c = 2 \times 10^{-9} \text{ m/s}$. Thus, melt could migrate for a distance of 2 mm over 300 hours. This is consistent with the observed scale of melt heterogeneity, indicating that the observed melt heterogeneity is likely caused by a temperature variation in the furnace.

Chapter 5: Conclusion

In this thesis work, I studied the patterns and mechanisms of the melt distribution in synthetic partially molten harzburgite samples. The samples are prepared by hot isostatic pressing a homogeneous mixture of oxides and natural, high-alumina basalt at upper mantle temperature (1350 °C) and pressure (1.5 GPa) conditions for durations of 42, 84, 168, 200, and 336 hours (Miller et al., 2016). After sintering, the samples were quenched and then cored into cylinders in the axial direction. The three-dimensional melt and mineral structure was detected using synchrotron-based X-ray microtomography and organized as a stack of grey-scale image slices.

For each sample, I cropped representative subvolumes, which cover an adequately large volume of the sample while avoiding the huge decompression cracks. The cropped gray-scale images were denoised and segmented to distinguish the melt and solid phases using different algorithms including the successive top-hat, watershed in Avizo[®] and a trainable machine learning segmentation in Fiji ImageJ.

For each subvolume, I measured the melt, opx and olivine fractions along or cross the axial direction. An increasing trend of melt fraction was observed along the vertical orientation in samples sintered longer than 84 hours. This indicates the melt fraction heterogeneity was generated during sintering and took more than 84 hours to develop. An analysis of mineral volume fractions suggested no systematic variations of opx/olivine distribution.

The importance of gravity as a driving force was first evaluated using the buoyancy-driven two-phase flow model proposed by McKenzie (1984). However, the scale of the observed melt variation and the speed at which they developed are not compatible with the calculation from the model. The buoyancy is not adequate to drive the melt migration in the sintering durations.

At grain scale ($\sim 50 \mu\text{m}$), surface tension can generate a pressure difference between melt and solid, which is three to four orders of magnitude larger than that produced by gravity and thus potentially be more efficient at driving melt migration. However, to drive the melt migration at sample scale ($\sim 1 \text{ mm}$), a variation in the solid-liquid interfacial energy γ_{sl} is needed. The variation of γ_{sl} is a linearly decreasing function of the temperature and depends on the materials that form the interface, i.e. mineral composition in our case. The experiment furnace is likely to have a temperature gradient of about $10^\circ\text{C}/\text{mm}$ over a distance of about 3 mm along the sample axis. The calculated melt migration velocity using the surface tension pressure as the driving force is still one magnitude smaller than the observation.

From the mineral distribution analysis, no systematic correlation between opx/olivine and melt volume fractions are observed, thus the lithologic partitioning is unlikely a major effect on the melt distribution.

Leshner and Walker (1988) demonstrated that thermal migration occurs in a temperature gradient and leads to olivine grain compaction and silica melt expulsion. Using the diffusion coefficient from Leshner and Walker (1988), I estimated a melt velocity of $2 \times 10^{-9} \text{ m/s}$ with a temperature gradient of $10^\circ\text{C}/\text{mm}$. With that velocity, melt can migrate 2 mm over 300 hours , which is consistent in magnitude with the

observed scale of melt heterogeneity. Thus, the patterns of melt distribution in the partially molten harzburgite samples are likely caused by a temperature gradient in the furnace through thermal migration.

Appendix A

Here I briefly review the equations governing the compaction of partially molten rocks. At initial condition ($t = 0$), the solid matrix is uniformly saturated with melt, i.e. the porosity is constant throughout the rock. The one-dimensional (1-D) governing equations of the compaction process are given as [e.g., McKenzie, 1984].

Mass conservation:

$$\frac{\partial \phi}{\partial t} = \frac{\partial}{\partial t}(\phi w) = 0 \quad (\text{A1})$$

$$\frac{\partial \phi}{\partial t} - \frac{\partial}{\partial t}[(1 - \phi)W] = 0 \quad (\text{A2})$$

Momentum conservation:

$$w - W = \frac{K}{\phi \mu} \frac{\partial P}{\partial z} \quad (\text{A3})$$

$$\frac{\partial P}{\partial z} + (1 - \phi)\Delta\rho g - \left(\zeta + \frac{4\eta}{3}\right) \frac{\partial^2 W}{\partial z^2} = 0 \quad (\text{A4})$$

Constitutive relation:

$$K = \frac{\phi^n D^2}{C} \quad (\text{A5})$$

The variables are defined in Table A1.

Eq (A1) and Eq (A2) give the mass conservation for the melt and matrix, respectively.

Eq (A3) is the Darcy's law in which the fluid pressure P comes from not only the buoyancy $\Delta\rho g$ but also the stress from the deforming matrix. Eq (A4) states the momentum conservation of the matrix with the assumption that the matrix is

compressible and has a bulk viscosity ζ . Eq (A5) is an empirical constitutive relation between permeability, porosity and the melt geometry.

Table A.1: Notations of variables used in McKenzie governing equations

Symbol	Definition
t	Time
z	Depth (positive upward)
ϕ	Porosity
w	Fluid velocity
W	Matrix velocity
P	Total pressure in the fluid
K	Permeability
μ	Shear viscosity of the fluid
$\Delta\rho$	Density difference between matrix and fluid
$\zeta=(1-\phi)\zeta^*$	Bulk viscosity of the aggregate, where ζ^* is the bulk viscosity of the solid phase
$\eta=(1-\phi)\eta^*$	Shear viscosity of the aggregate, where η^* is the shear viscosity of the solid phase
D	Grain size
C	Geometric factor influenced by the dihedral angle
n	Power law exponent
g	Acceleration due to gravity

Appendix B

The list of information of all analyzed subvolumes is provided in Table B.1. Figures B.1 to B.3 show the melt fraction profiles along the vertical axis of the associated core and Figures B.4 to B.7 the melt fraction profile along the horizontal axis of the associated core.

Table B.1: List of location, size, analysis directions and methods of all analyzed subvolumes. All subvolumes are cuboid. The locations are given in terms of the coordinated of two diagonal vertexes. The third dimension is parallel to the sample axis.

Subvolumes	(x1, y1, z1) ^a	(x8, y8, z8) ^a	Size ^b	Direction ^c	melt segmentation			opx segmentation			
					Top-hat	TSW	Watershed	TSW	Watershed	TSW	GrainSeparation
hzb-2-sub1	(501, 1101, 301)	(900, 1500, 1700)	400x400x1400	h	✓	✓	✓	✓	✓	✓	×
hzb-3-sub1	(400, 400, 471)	(750, 740, 1570)	351x351x1100	h	✓	×	×	×	×	×	×
hzb-5-sub1	(901, 201, 331)	(1500, 800, 1330)	600x600x1000	h/v	✓	✓	✓	✓	✓	✓	✓
hzb-5-sub2	(901, 1201, 331)	(1500, 1800, 1380)	600x600x1140	h/v	✓	×	×	×	✓	×	×
hzb-6-sub1	(1201, 1001, 560)	(1700, 1500, 819)	500x500x260	h/v	✓	✓	✓	✓	✓	✓	×
hzb-6-sub2	(1201, 1001, 819)	(1700, 1500, 1219)	500x500x401	h/v	✓	✓	✓	✓	✓	✓	×
hzb-6-sub3	(444, 1201, 1000)	(650, 1450, 1450)	207x250x460	h/v	✓	✓	✓	✓	✓	✓	×
hzb-6-sub4	(444, 294, 600)	(893, 438, 999)	450x145x400	h/v	✓	✓	✓	✓	✓	✓	×
hzb-7-sub1	(450, 1000, 356)	(949, 1499, 1555)	500x500x1200	h/v	✓	✓	✓	✓	✓	✓	×
hzb-7-sub2	(1100, 400, 376)	(1599, 899, 1465)	500x500x1090	h/v	✓	✓	✓	✓	✓	✓	×
hzb-7-sub3	(1001, 351, 290)	(1400, 750, 1419)	400x400x1130	h/v	✓	✓	✓	✓	✓	✓	×
hzb-9-sub1	(601, 601, 421)	(1050, 1050, 1650)	450x450x1230	h/v	✓	✓	✓	✓	✓	✓	×
hzb-9-sub2	(601, 1051, 1151)	(1050, 1500, 1650)	450x450x500	h/v	✓	×	×	×	×	×	×
hzb-10-sub1	(751, 1001, 1142)	(1250, 1500, 1515)	500x500x374	h/v	✓	✓	✓	✓	✓	✓	×
hzb-12-sub1	(501, 1001, 201)	(1100, 1600, 1510)	600x600x1310	h/v	✓	✓	✓	✓	✓	✓	×
hzb-12-sub2	(991, 1001, 1501)	(1530, 1540, 1700)	540x540x200	h/v	✓	×	×	×	×	×	×
hzb-13-sub1	(450, 450, 295)	(1249, 1249, 1684)	800x800x1390	h/v	✓	×	×	×	×	×	×
hzb-14-sub1	(501, 501, 112)	(1400, 1400, 1761)	900x900x1650	h/v	✓	✓	✓	✓	✓	✓	×
hzb-14-sub1.1	(501, 501, 112)	(950, 950, 1761)	450x450x1650	h/v	✓	✓	✓	✓	✓	✓	×
hzb-14-sub1.2	(951, 501, 112)	(1400, 950, 1761)	450x450x1650	h/v	✓	✓	✓	✓	✓	✓	×
hzb-14-sub1.3	(501, 951, 112)	(950, 1400, 1761)	450x450x1650	h/v	✓	✓	✓	✓	✓	✓	×
hzb-14-sub1.4	(951, 951, 112)	(1400, 1400, 1761)	450x450x1650	h/v	✓	✓	✓	✓	✓	✓	×
hzb-15-sub1	(400, 800, 230)	(799, 1199, 1829)	400x400x1600	h/v	✓	✓	✓	✓	✓	✓	✓
hzb-15-sub2	(600, 135, 170)	(999, 534, 769)	400x400x600	h/v	✓	✓	✓	✓	✓	✓	×
hzb-15-sub3	(528, 1440, 280)	(890, 1848, 1549)	363x409x1270	h/v	✓	✓	✓	✓	✓	✓	×
olox-1-sub1	(750, 1200, 311)	(1249, 1699, 1600)	500x500x1290	h/v	✓	×	×	×	×	×	×
olox-1-sub2	(421, 241, 1601)	(800, 600, 1847)	380x360x247	h/v	✓	×	×	×	×	×	×
olox-1-sub3	(481, 481, 290)	(1200, 1200, 1419)	720x720x1130	h/v	✓	×	×	×	×	×	×

^a All subvolume are cuboid and their locations are given by coordinates of diagonal vertexes in the whole original image stack (unit in pixels).

^b Size of each subvolume, unit in pixel.

^c Direction of analysis: “h” for horizontal and “v” for vertical.

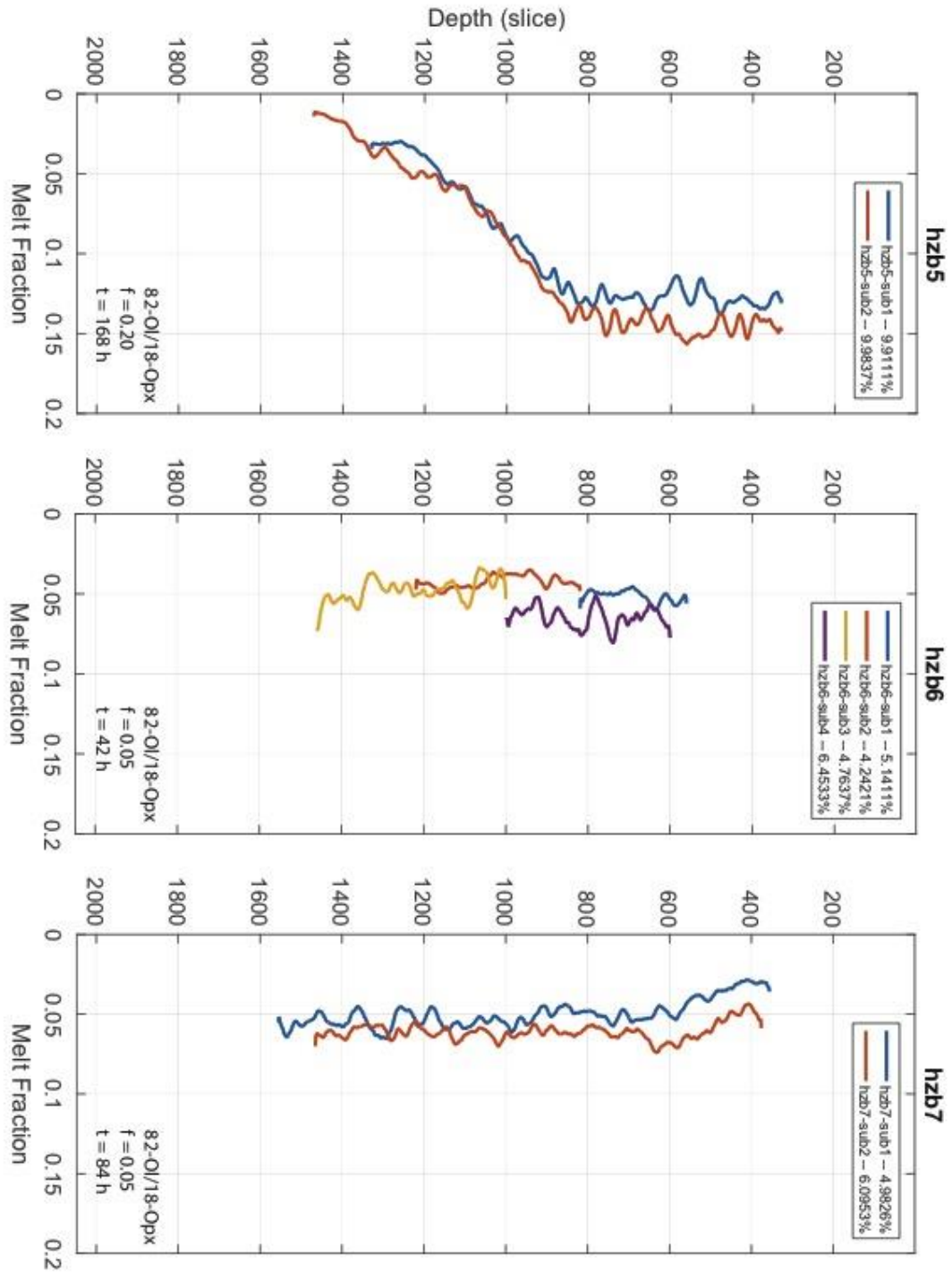


Figure B.1: Melt fraction profile along the vertical direction for subvolumes of samples hzb5, hzb6, and hzb7. Each depth slice is $0.74 \mu\text{m}$ thick and smoothing with a 21-slice kernel was applied to the profile. Each color corresponds to a different subvolume in the sample core.

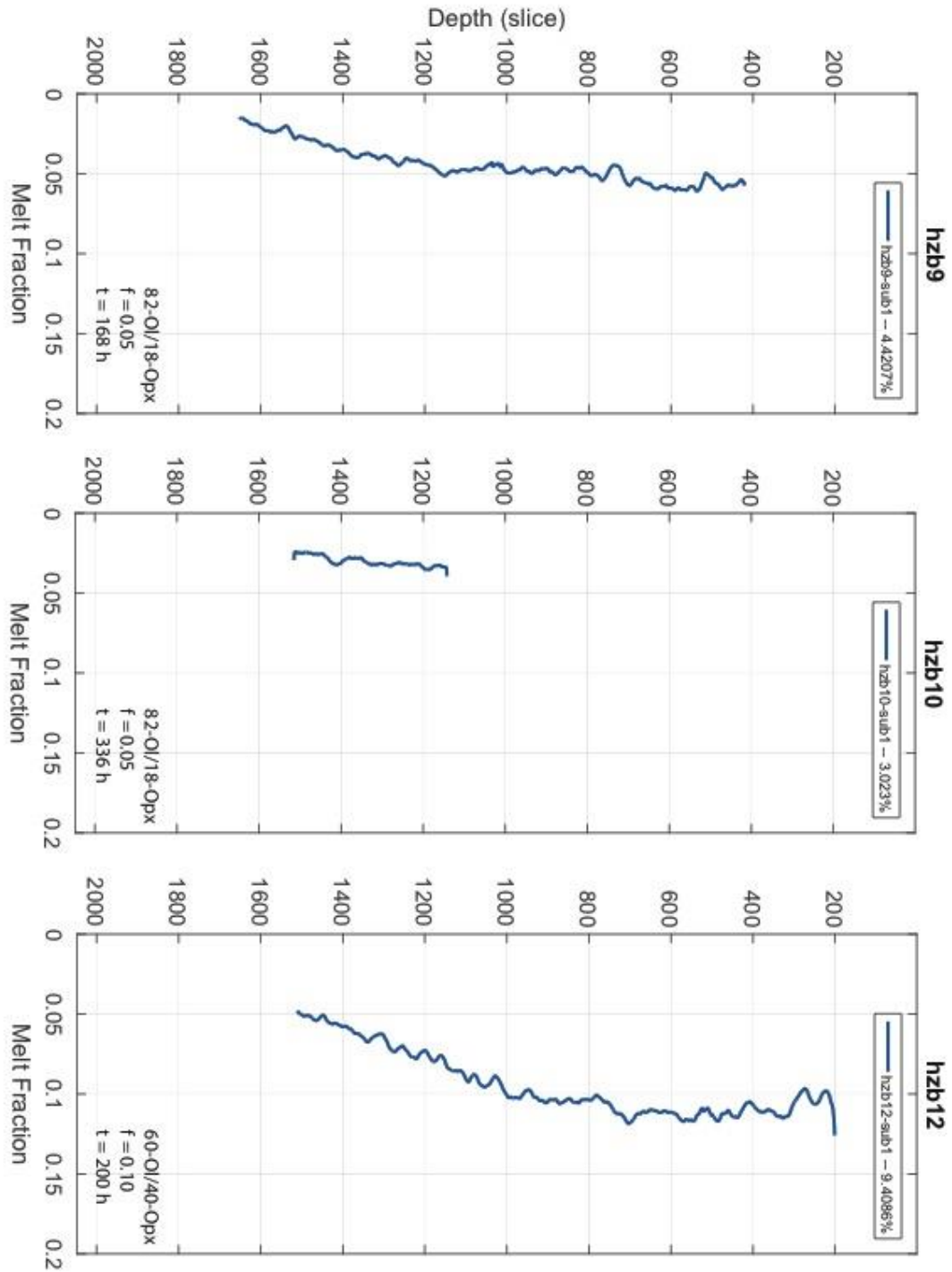


Figure B.2: Melt fraction profile along the vertical direction for subvolumes of samples hzb9, hzb10, and hzb12. Each depth slice is $0.74 \mu\text{m}$ thick and smoothing with a 21 slice kernel was applied to the profile.

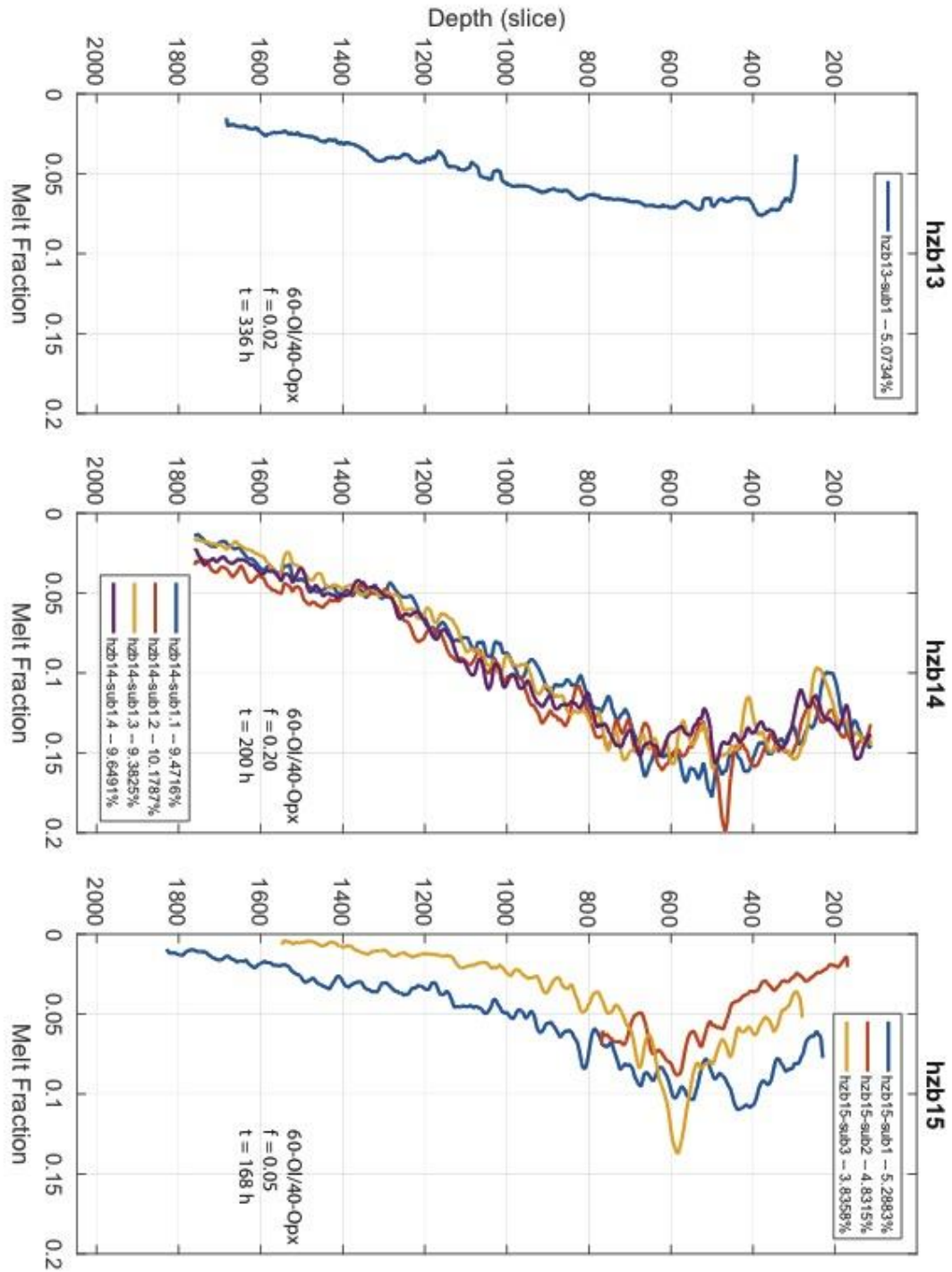


Figure B.3: Melt fraction profile along the vertical direction for subvolumes of samples hzb13, hzb14, and hzb15. Each depth slice is $0.74 \mu\text{m}$ thick and smoothing with a 21 slice kernel was applied to the profile. Each color corresponds to a different subvolume in the sample core.

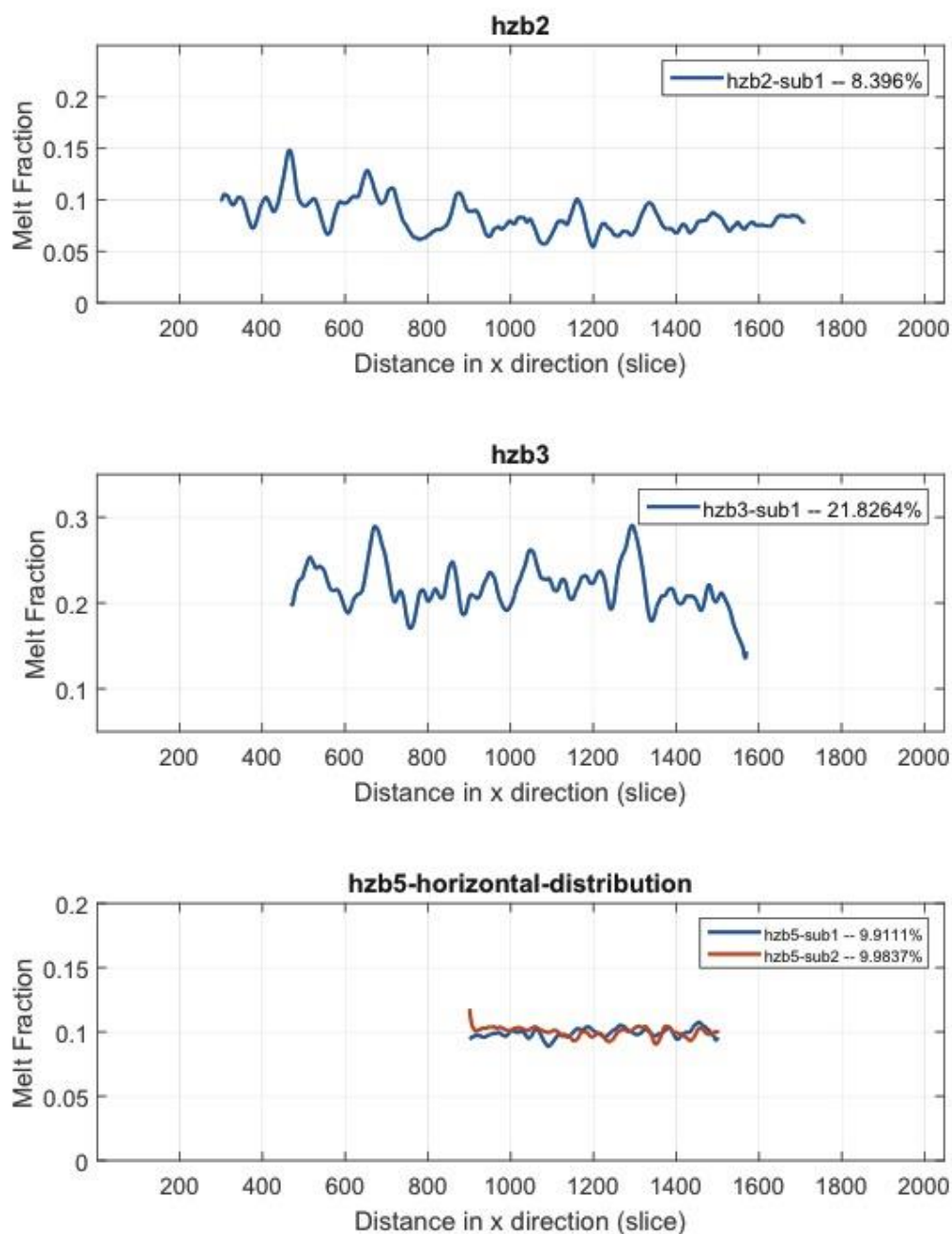


Figure B.4: Melt fraction profile along the horizontal direction for subvolumes of samples hzb2, hzb3, and hzb5. Each depth slice is $0.74 \mu\text{m}$ thick and smoothing with a 21 slice kernel was applied to the profile. Each color corresponds to a different subvolume in the sample core.

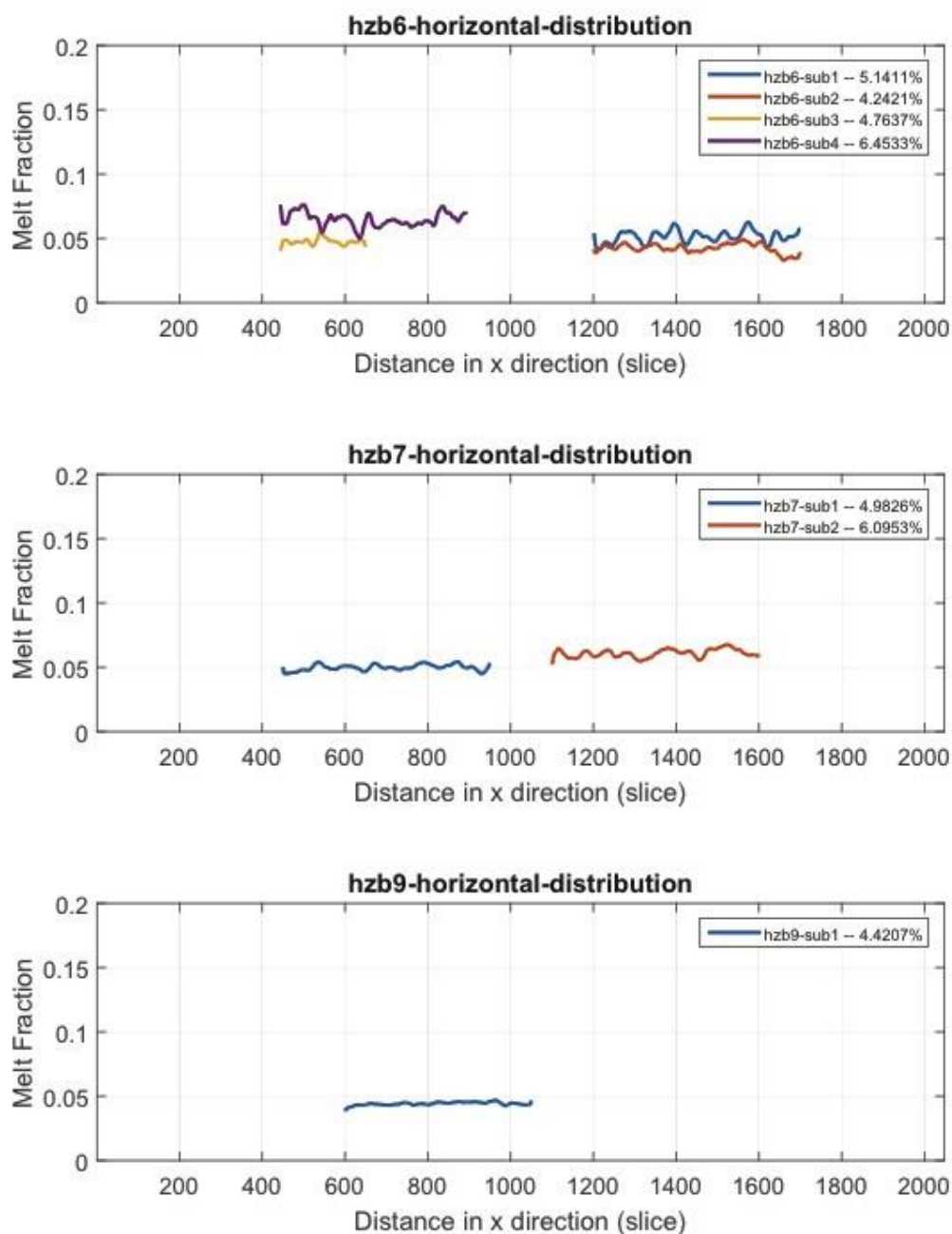


Figure B.5: Melt fraction profile along the horizontal direction for subvolumes of samples hzb6, hzb7, and hzb8. Each depth slice is $0.74 \mu\text{m}$ thick and smoothing with a 21 slice kernel was applied to the profile. Each color corresponds to a different subvolume in the sample core.

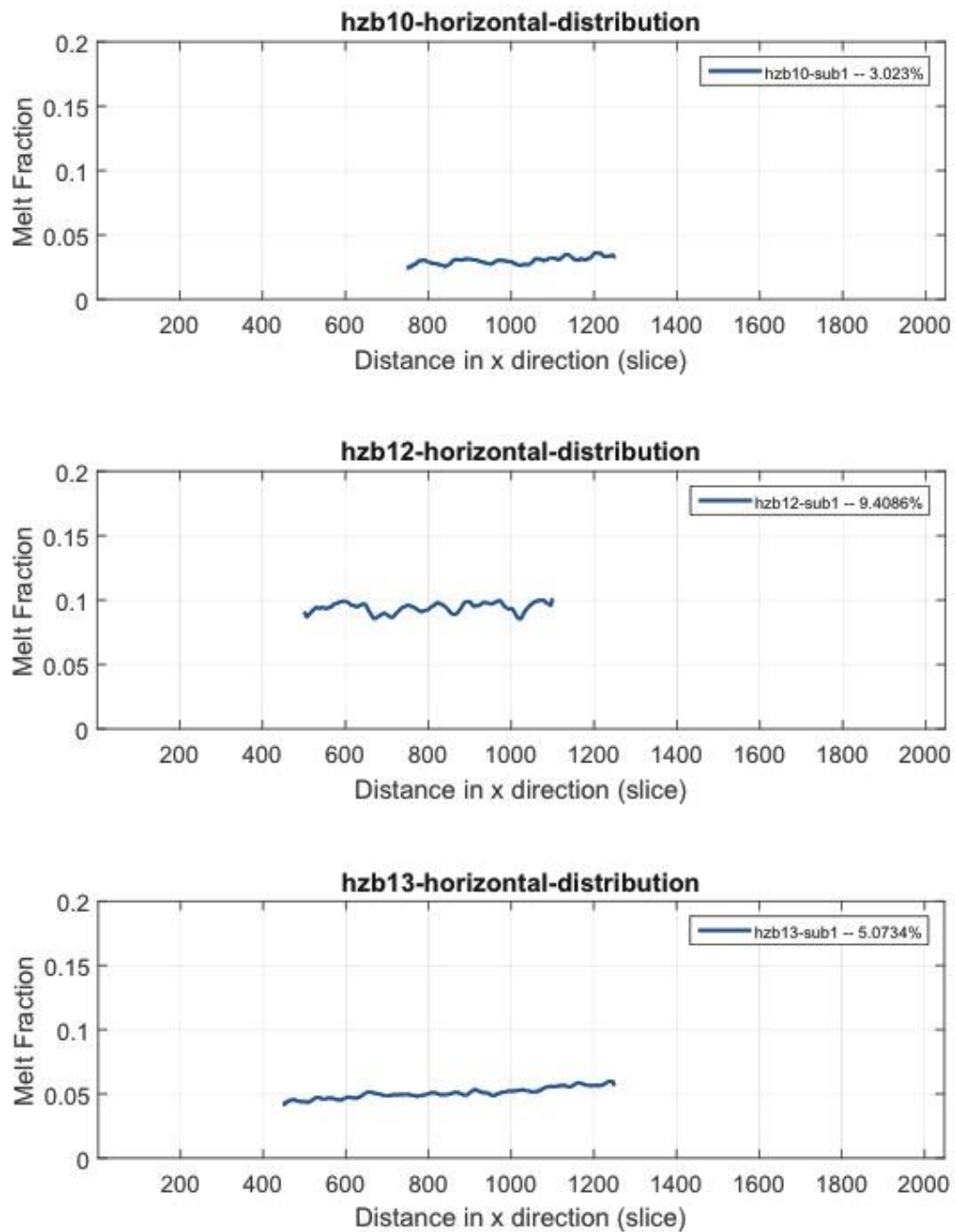


Figure B.6: Melt fraction profile along the horizontal direction for subvolumes of samples hzb10, hzb12, and hzb13. Each depth slice is $0.74 \mu\text{m}$ thick and smoothing with a 21 slice kernel was applied to the profile.

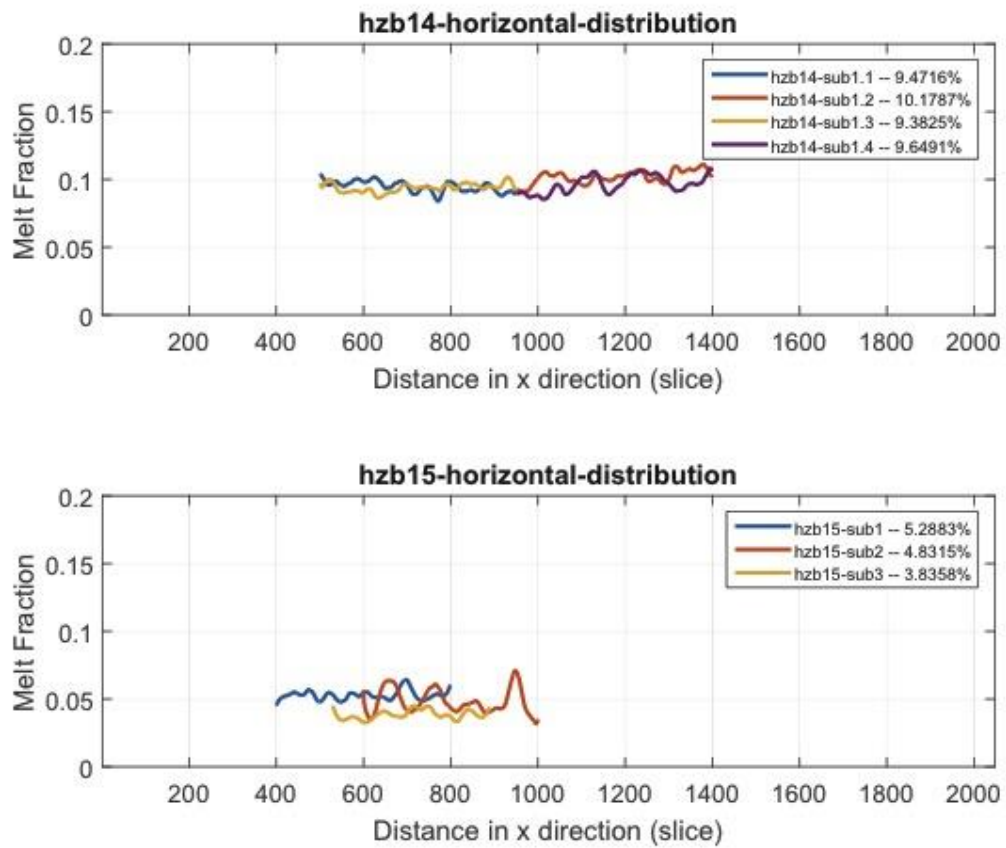


Figure B.7: Melt fraction profile along the horizontal direction for subvolumes of samples hzb14 and hzb15. Each depth slice is $0.74 \mu\text{m}$ thick and smoothing with a 21 slice kernel was applied to the profile. Each color corresponds to a different subvolume in the sample core.

Appendix C

A segmentation of melt/olivine/opx for hzb5-sub1 is obtained following the grain separation method from Miller et al. (2016). This method addresses the segmentation problem of olivine and opx by first separating all grains using the melt segmentation results and then manually selecting opx/olivine grains by their grayscale intensity. I applied this segmentation method to two of our samples subvolumes (hzb5-sub1 and hzb15-sub1) to better constrain the segmentation results. [Figure C.1 A](#) shows the grain separation of hzb5-sub1 and [Figure C.1 C](#) shows the manually selected opx phase. [Figure C.2](#) and [Figure C.3](#) compare the segmentation of grain separation method and TWS for hzb5-sub1 and hzb15-sub1, respectively. Although in the hzb5-sub1 segmentation, the grain separation method gives a lower opx fraction estimation, the overall trend of the mineral fractions are same for both subvolumes.

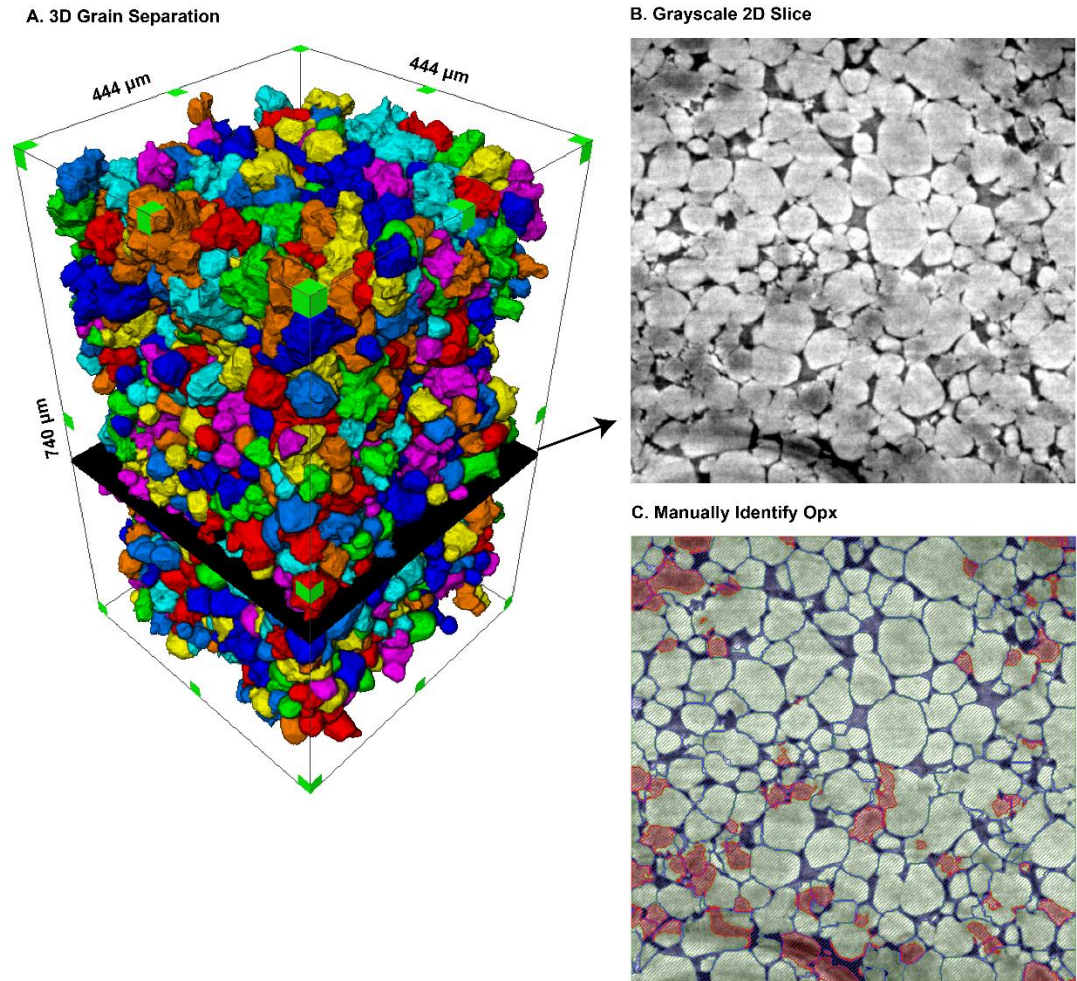


Figure C.1: Segmentation of hzb5-sub1 by Grain Separation. (A) 3D volume rendering of the separated grains. Grains intersected by the subvolume boundary are removed for better illustration. Size of the subvolume is labeled. (B) A 2D view of one of the slice in this subvolume. (C) 2D view of the grain separation (olivine in green) and manually selected opx phase (in red).

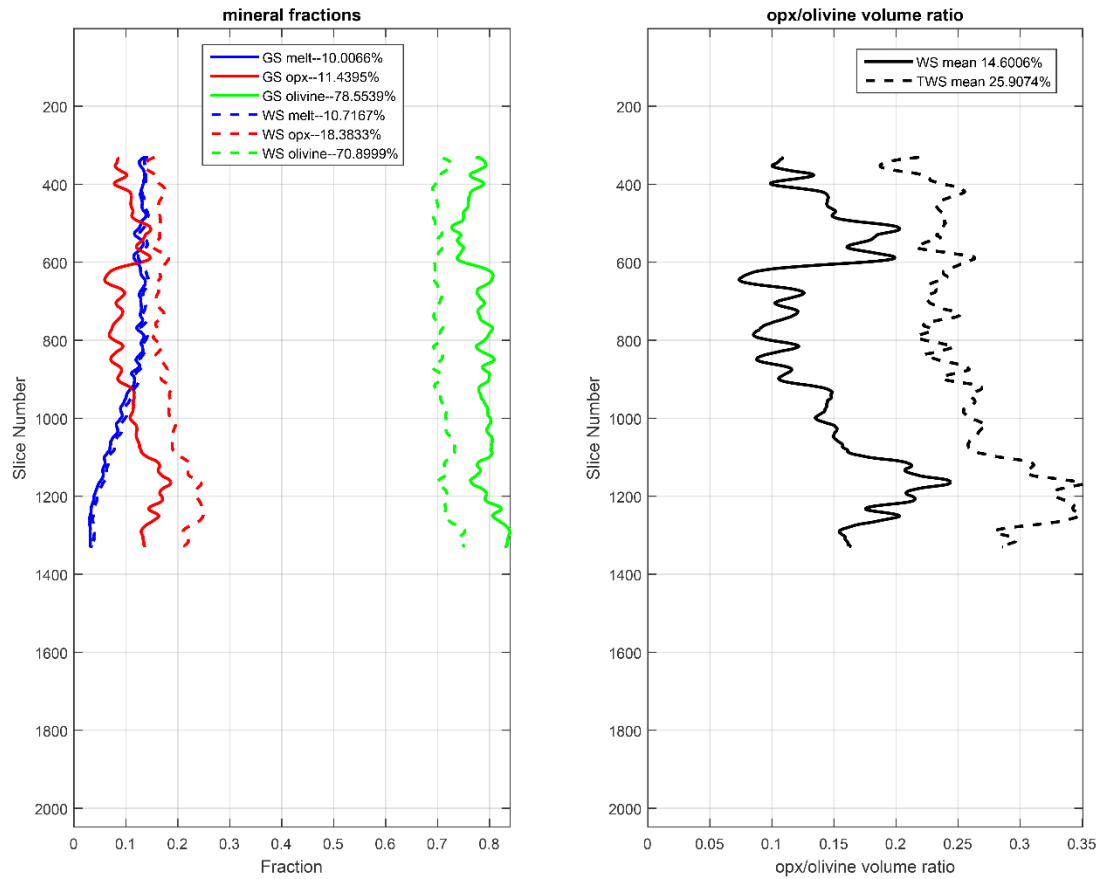


Figure C.2: Grain separation segmentation result of hzb5-sub1. Melt and mineral volume fractions are plotted for hzb5-sub1 along sample core axis. In the left panel, blue, red and green curves represent the volume fraction of melt, opx and olivine. In the right panel, the black curve represents the opx/olivine volumetric ratio along the core axis. In both panels, the solid curves are calculated from grain separation segmentation result and dashed ones from TWS. The fraction in the legend is the total volume fraction in that subvolume. The trend of opx fraction variation appears similar from both methods.

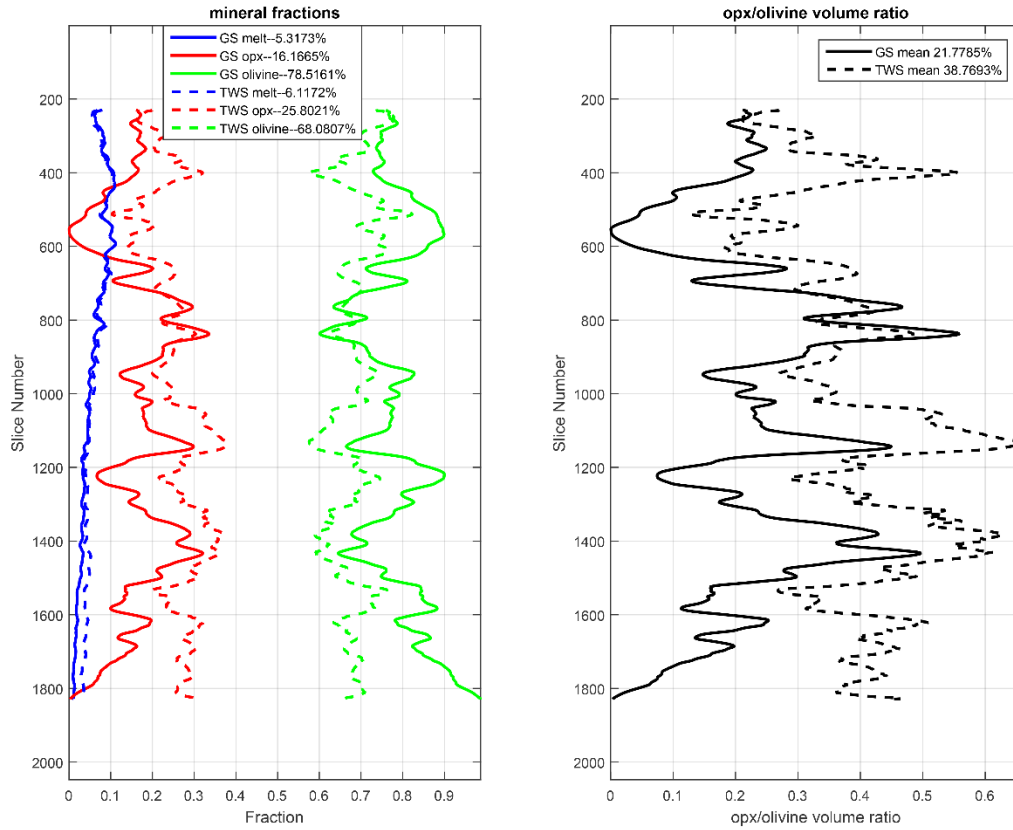


Figure C.3: Grain separation segmentation result of hzb15-sub1. Melt and mineral volume fractions are plotted for hzb15-sub1 along sample core axis. In the left panel, blue, red and green curves represent the volume fraction of melt, opx and olivine. In the right panel, the black curve represents the opx/olivine volumetric ratio along the core axis. In both panels, the solid curves are calculated from grain separation segmentation results and dashed ones from TWS. The fraction in the legend is the total volume fraction in that subvolume.

Bibliography

- Ahern, J., & Turcotte, D. L. (1979). Magma migration beneath an ocean ridge. *Earth and Planetary Science Letters*, 45(1), 115-122.
- Asimow, P. D., & Langmuir, C. H. (2003). The importance of water to oceanic mantle melting regimes. *Nature*, 421(6925), 815-820.
- Bai, H., & Montési, L. G. (2015). Slip-rate-dependent melt extraction at oceanic transform faults. *Geochemistry, Geophysics, Geosystems*, 16(2), 401-419.
- Bercovici, D., Ricard, Y., & Schubert, G. (2001). A two-phase model for compaction and damage: 1. General theory. *Journal of Geophysical Research: Solid Earth*, 106(B5), 8887-8906.
- Boas, F. E., & Fleischmann, D. (2012). CT artifacts: causes and reduction techniques. *Imaging in Medicine*, 4(2), 229-240.
- Buades, A., Coll, B., & Morel, J. M. (2005, June). A non-local algorithm for image denoising. In *2005 IEEE Computer Society Conference on Computer Vision and Pattern Recognition (CVPR'05)* (Vol. 2, pp. 60-65). IEEE.
- Bulau, J. R., Waff, H. S., & Tyburczy, J. A. (1979). Mechanical and thermodynamic constraints on fluid distribution in partial melts. *Journal of Geophysical Research: Solid Earth*, 84(B11), 6102-6108.
- Caldwell, D. R., & Eide, S. A. (1985). Separation of seawater by Soret diffusion. *Deep Sea Research Part A. Oceanographic Research Papers*, 32(8), 965-982.
- Cooper, R. F., & Kohlstedt, D. L. (1982). Interfacial energies in the olivine-basalt system. *Adv. Earth Planet. Sci*, 12, 217-228.
- Cooper, R. F., & Kohlstedt, D. L. (1984). Sintering of olivine and olivine-basalt aggregates. *Physics and Chemistry of Minerals*, 11(1), 5-16.
- Dasgupta, R., & Hirschmann, M. M. (2006). Melting in the Earth's deep upper mantle caused by carbon dioxide. *Nature*, 440(7084), 659-662.
- Drew, D. A. (1971). Averaged field equations for two-phase media. *Studies in Applied Mathematics*, 50(2), 133-166.
- Drew, D. A., & Segel, L. A. (1971). Averaged equations for two-phase flows. *Studies in Applied Mathematics*, 50(3), 205-231.
- Evans, R. L., Tarits, P., Chave, A. D., White, A., Heinson, G., Filloux, J. H., ... & Unsworth, M. J. (1999). Asymmetric electrical structure in the mantle beneath the East Pacific Rise at 17 S. *Science*, 286(5440), 752-756.
- Frank, F. C. (1968). Two-component flow model for convection in the Earth's upper mantle. *Nature*, 220, 350-352.
- Fusseis, F., Schrank, C., Liu, J., Karrech, A., Llana-Fúnez, S., Xiao, X., & Regenauer-Lieb, K. (2012). Pore formation during dehydration of a

- polycrystalline gypsum sample observed and quantified in a time-series synchrotron X-ray micro-tomography experiment. *Solid Earth*, 3(1), 71.
- Gale, A., Langmuir, C. H., & Dalton, C. A. (2014). The global systematics of ocean ridge basalts and their origin. *Journal of Petrology*, 55(6), 1051-1082.
- Gürsoy, D., De Carlo, F., Xiao, X., & Jacobsen, C. (2014). TomoPy: a framework for the analysis of synchrotron tomographic data. *Journal of synchrotron radiation*, 21(5), 1188-1193.
- Hall, M., Frank, E., Holmes, G., Pfahringer, B., Reutemann, P., & Witten, I. H. (2009). The WEKA data mining software: an update. *ACM SIGKDD explorations newsletter*, 11(1), 10-18.
- Harte, B., Hunter, R. H., & Kinny, P. D. (1993). Melt geometry, movement and crystallization, in relation to mantle dykes, veins and metasomatism. *Philosophical Transactions of the Royal Society of London A: Mathematical, Physical and Engineering Sciences*, 342(1663), 1-21.
- Holtzman, B. K., Groebner, N. J., Zimmerman, M. E., Ginsberg, S. B., & Kohlstedt, D. L. (2003). Stress - driven melt segregation in partially molten rocks. *Geochemistry, Geophysics, Geosystems*, 4(5).
- Holtzman, B. K., & Kohlstedt, D. L. (2007). Stress-driven melt segregation and strain partitioning in partially molten rocks: Effects of stress and strain. *Journal of Petrology*, 48(12), 2379-2406.
- Holtzman, B. K., Kohlstedt, D. L., Zimmerman, M. E., Heidelbach, F., Hiraga, T., & Hustoft, J. (2003). Melt segregation and strain partitioning: implications for seismic anisotropy and mantle flow. *Science*, 301(5637), 1227-1230.
- Huang, F., et al. "Chemical and isotopic fractionation of wet andesite in a temperature gradient: experiments and models suggesting a new mechanism of magma differentiation." *Geochimica et Cosmochimica Acta* 73.3 (2009): 729-749.
- Katz, R. F. (2008). Magma dynamics with the enthalpy method: Benchmark solutions and magmatic focusing at mid-ocean ridges. *Journal of Petrology*, 49(12), 2099-2121.
- Kelemen, P. B., Hirth, G., Shimizu, N., Spiegelman, M., & Dick, H. J. (1997). A review of melt migration processes in the adiabatically upwelling mantle beneath oceanic spreading ridges. *Philosophical Transactions of the Royal Society of London A: Mathematical, Physical and Engineering Sciences*, 355(1723), 283-318.
- Kelemen, P. B., Shimizu, N., & Salters, V. J. (1995). Extraction of mid-ocean-ridge basalt from the upwelling mantle by focused flow of melt in dunite channels. *Nature*, 375(6534), 747-753.
- Key, K., Constable, S., Liu, L., & Pommier, A. (2013). Electrical image of passive mantle upwelling beneath the northern East Pacific Rise. *Nature*, 495(7442), 499-502.
- Kohlstedt, D. L. (2002). Partial melting and deformation. *Reviews in mineralogy and geochemistry*, 51(1), 121-135.

- Kohlstedt, D. L., & Holtzman, B. K. (2009). Shearing melt out of the Earth: An experimentalist's perspective on the influence of deformation on melt extraction. *Annual Review of Earth and Planetary Sciences*, 37, 561-593.
- Langmuir, C. H., Klein, E. M., & Plank, T. (1993). Petrological systematics of mid-ocean ridge basalts: Constraints on melt generation beneath ocean ridges. *Mantle flow and melt generation at mid-ocean ridges*, 183-280.
- Leshner, C. E., and D. Walker. "Cumulate maturation and melt migration in a temperature gradient." *Journal of Geophysical Research: Solid Earth* 93.B9 (1988): 10295-10311.
- Leshner, C. E. (1986). Effects of silicate liquid composition on mineral- liquid element partitioning from Soret diffusion studies. *Journal of Geophysical Research: Solid Earth*, 91(B6), 6123-6141.
- Leshner, C. E., and D. Walker. "Solution properties of silicate liquids from thermal diffusion experiments." *Geochimica et Cosmochimica Acta* 50.7 (1986): 1397-1411.
- McKenzie, D. P. (1969). Speculations on the consequences and causes of plate motions. *Geophysical Journal International*, 18(1), 1-32.
- McKenzie, D. (1984). The generation and compaction of partially molten rock. *Journal of Petrology*, 25(3), 713-765.
- Miller, K. J., Zhu, W. L., Montési, L. G., & Gaetani, G. A. (2014). Experimental quantification of permeability of partially molten mantle rock. *Earth and Planetary Science Letters*, 388, 273-282.
- Montesi, L. G., Behn, M. D., Hebert, L. B., Lin, J., & Barry, J. L. (2011). Controls on melt migration and extraction at the ultraslow Southwest Indian Ridge 10–16 E. *Journal of Geophysical Research: Solid Earth*, 116(B10).
- Niu, Y. (1997). Mantle melting and melt extraction processes beneath ocean ridges: evidence from abyssal peridotites. *Journal of Petrology*, 38(8), 1047-1074.
- Park, H. H., & Yoon, D. N. (1985). Effect of dihedral angle on the morphology of grains in a matrix phase. *Metallurgical Transactions A*, 16(5), 923-928.
- Platten, J. K., Bou-Ali, M. M., Costesèque, P., Dutrieux, J. F., Köhler, W., Leppla, C., ... & Wittko, G. (2003). Benchmark values for the Soret, thermal diffusion and diffusion coefficients of three binary organic liquid mixtures. *Philosophical Magazine*, 83(17-18), 1965-1971.
- Reid, I., & Jackson, H. R. (1981). Oceanic spreading rate and crustal thickness. *Marine Geophysical Researches*, 5(2), 165-172.
- Renner, J., Viskupic, K., Hirth, G., & Evans, B. (2003). Melt extraction from partially molten peridotites. *Geochemistry, Geophysics, Geosystems*, 4(5).
- Ricard, Y., Bercovici, D., & Schubert, G. (2001). A two-phase model for compaction and damage. II- Applications to compaction, deformation, and the role of interfacial surface tension. *Journal of geophysical research*, 106(B5), 8907-8924.

- Riley, G. N., & Kohlstedt, D. L. (1991). Kinetics of melt migration in upper mantle-type rocks. *Earth and Planetary Science Letters*, 105(4), 500-521.
- Riley, G. N., Kohlstedt, D. L., & Richter, P. M. (1990). Melt migration in a silicate liquid-olivine system: An experimental test of compaction theory. *Geophysical Research Letters*, 17(12), 2101-2104.
- Scott, D. R., & Stevenson, D. J. (1986). Magma ascent by porous flow. *Journal of Geophysical Research: Solid Earth*, 91(B9), 9283-9296.
- Sleep, N. H. (1974). Segregation of magma from a mostly crystalline mush. *Geological Society of America Bulletin*, 85(8), 1225-1232.
- Sparks, D. W., & Parmentier, E. M. (1991). Melt extraction from the mantle beneath spreading centers. *Earth and Planetary Science Letters*, 105(4), 368-377.
- Spiegelman, M., & McKenzie, D. (1987). Simple 2-D models for melt extraction at mid-ocean ridges and island arcs. *Earth and Planetary Science Letters*, 83(1), 137-152.
- Spiegelman, M., Kelemen, P. B., & Aharonov, E. (2001). Causes and consequences of flow organization during melt transport: The reaction infiltration instability in compactible media. *Journal of Geophysical Research: Solid Earth*, 106(B2), 2061-2077.
- Spiegelman, M., & Kelemen, P. B. (2003). Extreme chemical variability as a consequence of channelized melt transport. *Geochemistry, Geophysics, Geosystems*, 4(7).
- Stevenson, D. J. (1989). Spontaneous small-scale melt segregation in partial melts undergoing deformation. *Geophysical Research Letters*, 16(9), 1067-1070.
- Toomey, D. R., Wilcock, W. S., Solomon, S. C., Hammond, W. C., & Orcutt, J. A. (1998). Mantle seismic structure beneath the MELT region of the East Pacific Rise from P and S wave tomography. *Science*, 280(5367), 1224-1227.
- Turner, A. J., Katz, R. F., & Behn, M. D. (2015). Grain-size dynamics beneath mid-ocean ridges: Implications for permeability and melt extraction. *Geochemistry, Geophysics, Geosystems*, 16(3), 925-946.
- Turcotte, D. L., & Schubert, G. (2014). *Geodynamics*. Cambridge University Press.
- Waff, H. S., & Bulau, J. R. (1979). Equilibrium fluid distribution in an ultramafic partial melt under hydrostatic stress conditions. *Journal of Geophysical Research: Solid Earth*, 84(B11), 6109-6114.
- Walker, D., & Agee, C. B. (1988). Ureilite compaction. *Meteoritics*, 23(1), 81-91.
- Woodbury, G. (1997). *Physical Chemistry*, Brooks. Cole, Pacific Grove.
- Walker, D., & DeLong, S. E. (1982). Soret separation of mid-ocean ridge basalt magma. *Contributions to Mineralogy and Petrology*, 79(3), 231-240.
- Witten, I. H., & Frank, E. (2005). *Data Mining: Practical machine learning tools and techniques*. Morgan Kaufmann.

Zhu, W., Gaetani, G. A., Fuisseis, F., Montési, L. G., & De Carlo, F. (2011). Microtomography of partially molten rocks: three-dimensional melt distribution in mantle peridotite. *Science*, 332(6025), 88-91.